JGR Earth Surface

RESEARCH ARTICLE
10.1029/2025JF008561

Anisotropic Stress History Effects in Erodible Sediment Beds

Sophie Bodek[1], Dong Wang[2], Mark D. Shattuck[3], Corey S. O'Hern[2,4,5], and Nicholas T. Ouellette[1]

[1]Department of Civil and Environmental Engineering, Stanford University, Stanford, CA, USA, [2]Department of Mechanical Engineering, Yale University, New Haven, CT, USA, [3]Benjamin Levich Institute and Physics Department, The City College of New York, New York, NY, USA, [4]Department of Applied Physics, Yale University, New Haven, CT, USA, [5]Department of Physics, Yale University, New Haven, CT, USA

Key Points:

- We use particle tracks from laboratory experiments to study grain velocities and activity subject to fluid flows from different directions
- Our sand bed strengthens under unidirectional flows, but exhibits weakening as the angle between "conditioning" and eroding flows increases
- The stress history imparted by directional flows impacts both the number of active grains and bedload velocity

Correspondence to:
S. Bodek,
sbodek@stanford.edu

Citation:
Bodek, S., Wang, D., Shattuck, M. D., O'Hern, C. S., & Ouellette, N. T. (2026). Anisotropic stress history effects in erodible sediment beds. *Journal of Geophysical Research: Earth Surface*, *131*, e2025JF008561. https://doi.org/10.1029/2025JF008561

Received 5 MAY 2025
Accepted 18 DEC 2025

Abstract Bedload transport occurs when the shear stress, or non-dimensional Shields stress, imparted by a fluid onto a sediment bed exceeds a critical value for sediment entrainment. The history of fluid stress imparted onto a sediment bed influences this critical Shields stress, with bed strengthening occurring under unidirectional flows and bed weakening occurring when the flow direction is reversed. In this study, we examine directional strengthening and weakening in a sediment bed for multiple fluid stress orientations using a rotating bed of sand in a laboratory flume. This sediment bed is exposed to an initial subcritical conditioning flow followed by a subsequent erosive flow at an offset angle of 0°, 45°, 90°, 135°, or 180°. We identify the particle trajectories of a population of sediment grains to measure their velocity, activity, and associated bulk statistics. We confirm bed strengthening (i.e., lower grain velocity and activity) in the unidirectional case, especially for flows at or below the nominal critical Shields stress. As the angular offset increases between the conditioning and erosive flows, both grain velocity and activity increase, with the greatest bed weakening at offsets of 135° and 180°. Our results confirm that stress history is stored anisotropically in the sediment bed, supporting mechanisms such as shear jamming where an anisotropic granular fabric develops in response to shear. These results inform our understanding of how subcritical and critical fluid-imposed stresses can modify the grain contact and force networks in geophysical contexts.

Plain Language Summary Bedload transport, or the movement of sediment near the surface of a sand or gravel bed, occurs when shearing forces delivered by a flowing fluid overcome the forces keeping the sediment in place. The critical shear stress depends on many variables, including the history of fluid flow over the bed. Sustained low flows can strengthen a sediment bed, resulting in reduced bedload transport and a higher critical shear stress, even when the bed appears mostly static. Recent studies have also shown that a low flow in one direction, followed by a higher flow in the opposite direction, results in bed weakening and greater bedload transport. To explore the influence of flow history and direction on critical shear stress, we use a laboratory flume with a rotating sediment bed. This sediment bed is subjected to a low flow, then rotated to a set angle and exposed to an erosive flow. We identify the tracks of individual sediment grains to analyze grain velocity and activity. We can then quantify the differences in sediment bed behavior, and we find that stress history imparted by previous flow directions leads to an anisotropic response in the sediment bed.

1. Introduction

The transport of sediment by flowing water is a fundamental physical process that shapes many of Earth's landscapes and has broad implications in environmental, ecological, and engineering contexts. The accurate prediction and evaluation of sediment transport thresholds and rates, however, remains an ongoing challenge due to the complex interactions between the granular bed material and turbulent, open-channel flow (see Pähtz et al., 2020). The typical framework for predicting the onset of sediment motion relies on an estimate of the Shields stress τ_*, the ratio of the fluid-imposed bed stress to the buoyancy-reduced gravitational stress (Shields, 1936). When the Shields stress reaches a critical value, τ_{*cr} (a threshold that is also dependent on the particle Reynolds number), sediment grains begin to be mobilized into bedload transport as the forces imposed by the driving fluid overcome those resisting entrainment (e.g., Dey, 1999; Wiberg & Smith, 1987). Although choosing a single value for this threshold of motion has significant utility and is widely assumed in bedload transport models (e.g., Ashida & Michiue, 1973; Engelund & Fredsøe, 1976; Luque & Van Beek, 1976; Meyer-Peter & Müller, 1948; Wong & Parker, 2006), challenges arise due to the considerable variation in reported shear stresses at the onset of sediment transport in both field and flume studies (Buffington & Montgomery, 1997) and

the diminished predictive power of these models near the threshold of grain motion (Recking et al., 2012). Thus, this framework, while useful, is ultimately insufficient in many contexts (e.g., Lavelle & Mofjeld, 1987; Yager et al., 2018).

The variable nature of the bed surface (e.g., Kirchner et al., 1990) and turbulent fluctuations in the flow (e.g., Einstein & El-Samni, 1949) give rise to complex physical mechanisms governing sediment entrainment and transport that can be highly variable across spatial and temporal scales (Cameron et al., 2020; Diplas et al., 2008; Escauriaza et al., 2023; Papanicolaou et al., 2001; Sumer et al., 2003). This temporal variability has been observed in both experimental and natural systems, where τ_{*cr} varies with the history of fluid stress (e.g., Mao, 2018; Turowski et al., 2011). Hysteresis can occur in sediment transport rates during individual floods (Mao et al., 2014; Pretzlav et al., 2020; Roth et al., 2014) and cause variations in the onset of sediment motion due to seasonal variability in flood magnitudes and intermittency (Masteller et al., 2019; Reid et al., 1985). Alternate representations of the critical Shields stress may assist in understanding these time-dependent dynamics. Clark et al. (2017) interpreted τ_{*cr} as the stress at which mobile grains can no longer find a static configuration—an approach that incorporates inertial effects from particle-bed interactions. Houssais et al. (2015), meanwhile, interpreted τ_{*cr} as the transition from creep to a dense granular flow, thus showing the presence of slow and sporadic grain movements within both the bed surface and subsurface.

While the traditional framework for estimating the onset of sediment transport assumes that granular beds do not undergo significant reorganization when the bed stress is below the threshold for bulk motion (Gomez, 1983), both field observations and laboratory experiments have shown that τ_{*cr} is sensitive to the magnitude and duration of prior flows, with beds typically exhibiting a strengthening behavior when the fluid flow always comes from the same direction, even in the absence of measurable sediment transport (An et al., 2021; Haynes & Pender, 2007; Masteller & Finnegan, 2017; Masteller et al., 2019; Monteith & Pender, 2005; Oldmeadow & Church, 2006; Ockelford & Haynes, 2013; Ockelford et al., 2019; Paphitis & Collins, 2005; Reid et al., 1985; Yang et al., 2024). The term *stress history* (also occasionally called *memory stress*) generally describes the effects of these sub-threshold flows applied to a sediment bed, and incorporates both the duration and magnitude of shear stress applied to the bed (Monteith & Pender, 2005); these sub-threshold flows are frequently referred to as "antecedent" flows (e.g., Monteith & Pender, 2005; Ockelford & Haynes, 2013) or "conditioning" flows (e.g., An et al., 2021; Galanis et al., 2022).

Previous research investigating stress history effects has primarily focused on gravel-bed rivers or used graded bed material in flume studies. Notably, Paphitis and Collins (2005) used a uniform sand bed when conducting flume experiments, finding that τ_{*cr} increased with longer sub-critical conditioning flow durations, and that τ_{*cr} also increased with greater conditioning flow stress—up to 95% of the nominal critical shear stress. Subsequent experiments using uniform bed material, although not sand-sized, reported similar findings with a reduction in bedload transport rates and increase in τ_{*cr} with longer inter-event subcritical flows (Ockelford et al., 2019). In geophysical contexts, the mechanism for strengthening in uniform beds subject to subcritical flows has generally been attributed to subtle reorganization of the sediment bed, leading to greater compaction or settling of the bed material and more stable grain configurations (e.g., Ockelford & Haynes, 2013). While these and similar mechanisms are also present in graded gravel beds (An et al., 2021; Haynes & Pender, 2007; Masteller & Finnegan, 2017), the relative influence of local repositioning (e.g., pivoting of grains into stable pockets) and settling of bed material (e.g., fines percolating into the subsurface) differs from uniform cases (Ockelford & Haynes, 2013).

We can also consider stress history as a type of strain hardening, as beds experience compaction when driven as bedload by above-critical flows (Charru et al., 2004) and as creep by subcritical flows (Allen & Kudrolli, 2018). Additionally, as the bed experiences a directional boundary shear, grain contacts can be preferentially loaded forming anisotropic force chains that bear internal stresses and stabilize the material in the direction of shear (Behringer & Chakraborty, 2018; Bi et al., 2011; Cates et al., 1998; Majmudar & Behringer, 2005). Continued loading can produce a fragile, then shear jammed state—conditions where the stability of the granular material can be disrupted if the direction of loading changes (Bi et al., 2011). In systems with cyclic shear, the grain network must rearrange upon change of direction of the applied shear, which further motivates weakening (Slotterback et al., 2012). Recent experiments examining the evolution of τ_{*cr} in granular beds subject to forward and reverse fluid shear directions have observed bed weakening (i.e., lower τ_{*cr} or increased bedload transport) when the flow direction is reversed (Cúñez et al., 2022; Galanis et al., 2022). Cúñez et al. (2022), who also

examined stress history effects from an oscillating flow, found that the granular fabric developed during the oscillating flow was weaker than the anisotropic fabric developed under unidirectional flow, despite greater compaction of the bed material.

Previous studies examining the development of stress history broadly fall into two categories: those motivated by geophysical settings like gravel-bed rivers, which often use unidirectional flows over graded sediment beds (e.g., An et al., 2021; Monteith & Pender, 2005), and those investigating grain-scale dynamics and mechanisms for storing memory stress, which tend to use monodisperse spherical beads (e.g., Allen & Kudrolli, 2018; Cúñez et al., 2022). In this article, we use elements from both categories to investigate the effect of directional stress history on thresholds for incipient grain motion in a uniform sediment bed consisting of natural sand grains exposed to a turbulent shear flow. We carry out experiments in a laboratory flume where the sediment bed is subject to a subcritical conditioning flow, followed by an erosive flow from an offset direction. While previous studies were limited to examining the evolution of bed stability subject to unidirectional and reversed flows, our experimental setup allows for mobilizing flow directions that are offset by any angle from the initial subcritical flow direction. By examining grain motions during the transition from below threshold to incipient motion to bedload transport, we are able to quantify grain velocity and activity. Further, we use collective grain velocity statistics to compare the number of mobilized grains and characteristic grain velocity for various conditioning directions. Our results imply that bedload transport may be enhanced when water-worked sediment beds are exposed to flow from multiple directions compared to predictions that use a standard Shields framework or even models that take unidirectional flow history into account (e.g., Masteller et al., 2025; Paphitis & Collins, 2005).

2. Methods

2.1. Experimental Configuration and Protocol

Experiments were conducted in a recirculating, open channel flume. The inflow is controlled by a variable speed pump that fills a constant-head tank, which drives the water through a diffuser, homogenizing grids, and a two-dimensional constriction into a rectangular channel section. The glass-walled test section has a length of 3 m and width of 0.6 m, with additional 1.5 m long buffer sections to mitigate entrance and exit effects. The flow rate and depth are set by both the pump and the height of a sharp-crested downstream control weir. At rest, the flow depth was 17.5 cm. Due to the fixed height of the control weir, the depth of water in the test section becomes deeper with increasing pump output; however, the water depth did not change by more than 4 cm over the range of pump settings used for experiments. A full description of this facility was initially documented in O'Riordan et al. (1993) and an illustrative schematic is shown in Figure 1a.

The test section of the flume has a false bottom, allowing for the installation of an inset sediment bed, the edge of which was mounted flush with the surrounding floor (Figure 1b). The leading edge was 1.3 m from the start of the test section, and the inset bed was centered within the channel cross section. The sediment bed consisted of a circular dish that was 45.7 cm (18 in) in diameter and 7.6 cm (3 in) deep; the dish was filled with medium to coarse-sized quartz sand ($D_{50} = 0.495$ mm; $\rho_s = 2650$ kg/m^3). The sand was sieved to constrain the minimum and maximum grain sizes (0.3 mm to 0.8 mm) and to produce a uniform grain size distribution with $\sigma_g = (D_{84}/D_{16})^{0.5} = 1.24$, as measured using a Camsizer X2 instrument (García, 2013). A sub-population of grains was spray-painted fluorescent orange for imaging purposes and mixed with the unpainted sand in a 17/83 mixture by volume (Figure 1c). The granular bed imaging and tracking methodologies are discussed further in Section 2.3. The sediment bed was mounted on a rotating turntable base, permitting multiple orientations of the sand bed relative to the flume.

A camera was mounted above the center of the sediment bed to record the motions of the sand grains. Any secondary flows produced by the transition between the smooth acrylic floor and the start of the sediment bed decayed before reaching the camera field of view (FOV), located 16 cm from the leading edge of the bed. To ensure that the camera had a clear view of the sand below, a small glass window (referred to as the "boat") was placed on the free surface of the flow above the sediment bed. This placement minimized image distortions due to light refraction off ripples in the free surface. An acoustic Doppler velocimeter (ADV) was mounted behind the boat over the downstream portion of the sediment bed to collect flow velocity measurements. The test section configuration is shown in Figures 1b and 1c.

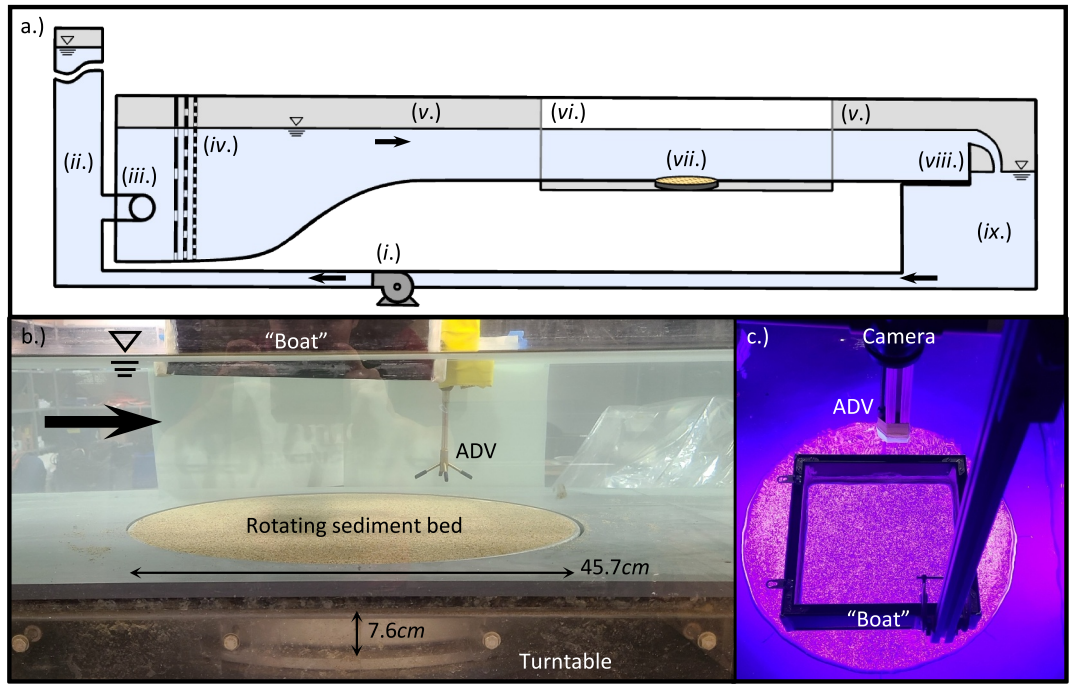

Figure 1. Recirculating flume facility with installed sediment bed. (a) Schematic depicting the entire flume facility, including: (i) variable-speed pump, (ii) constant-head tank, (iii) diffuser and inlet, (iv) homogenizing grids, (v) 1.5 m long buffer sections, (vi) 3 m long glass-walled test section, (vii) inset rotating sediment bed, (viii) sharp-crested control weir, and (ix) reservoir. (b) Close-up of the portion of the test section with the inset sediment bed and nearby instrumentation. (c) Top-down view of the sediment bed illuminated by ultraviolet lights, showing the fluorescent-painted grains.

We were careful to prepare the sediment bed in the same way for each experimental run. Prior to each experiment, a stirrer was used to agitate the submerged sand bed and break up any structures that may have been present within the granular material. We then leveled the sediment bed by dragging a stiff piece of mesh over the bed surface in the downstream direction. For all experimental cases except the control, we then subjected the bed to a subcritical "conditioning flow" for 20 min. Previous studies have observed strengthening in sand-sized bed material after conditioning flows as short as 5–6 min (Galanis et al., 2022; Paphitis & Collins, 2005); additionally, experiments involving graded gravel beds show the greatest adjustment in bed topography over the first 15 min of conditioning (An et al., 2021). We confirm the efficacy of a 20 min conditioning flow by fitting an exponential decay function to measures of grain mobility, which reveal that the sediment bed experiences a 50% reduction in grain velocity and activity within approximately 5 min of the start of the conditioning period (see Section 3.1). This conditioning flow had a Shields number that was approximately 75−80% of the nominal critical value for our sediment bed. The critical value, $\tau_{*cr} \approx 0.033$, was estimated by plotting τ_* and particle Reynolds number Re_p determined for various pump settings on the Shields curve (Vanoni, 2006) and then interpolating the τ_{*cr} value where these points and the Shields curve intersect. Flow characterization used to calculate τ_* and Re_p is discussed further in Section 2.2. Although several grains were observed to jiggle or even roll one or two grain diameters during the course of the conditioning period, significant grain motion was not observed at this flow velocity.

Following this 20 min period, we stopped the flow and—without draining the flume—manually rotated the sand bed by 0°, 45°, 90°, 135°, or 180° relative to the initial conditioning flow direction. In addition to the five angles tested, we also tested a control case that was not subject to the 20 min conditioning period. Given that the conditioning flow was sub-threshold with minimal sediment transport observed, the act of stopping the flow and slowly turning the submerged bed is not expected to have a significant impact on the ensuing sediment transport dynamics. The rotating sediment bed apparatus was otherwise stationary during both the conditioning phase and the subsequent "erosive flow". The rotation thus only changed the direction of the erosive flow relative to the initial conditioning flow.

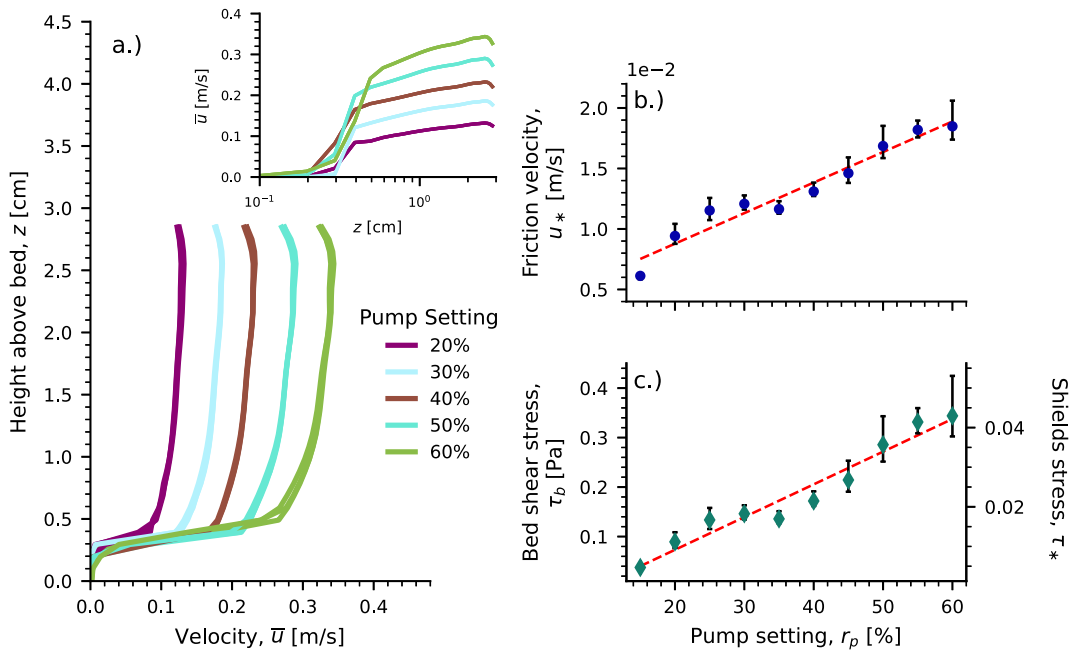

Figure 2. (a) Measured time-averaged velocity profiles for 5 pump settings used to calibrate flow parameters; the pump setting value indicates the percentage of the maximum pump output. The inset shows the same data plotted using semi-logarithmic axes, with the friction velocity u_* as the slope of the log-law region of the profile. (b) u_* computed for each pump setting using the Law of the Wall. The red dashed line indicates a linear best fit given by $u_* = 2.5 \times 10^{-4}\, r_p + 3.7 \times 10^{-3}$. (c) Bed shear stress τ_b and Shields stress τ_* as a function of pump setting. The red dashed line indicates a linear best fit given by $\tau_b = 6.6 \times 10^{-3}\, r_p - 5.9 \times 10^{-2}$. Error bars indicate the range of values calculated.

To produce the erosive flow, the speed of the pump was raised in a series of steps with a total of 9 flow velocity intervals used when inducing sediment transport—starting at the conditioning flow velocity ($\tau_* = 0.026$) and increasing to an above-threshold state where bedload was readily observed ($\tau_* = 0.05$). After each step up, the flow was allowed to stabilize for 1 min, after which a 45 sec video of the sediment motions was collected. The entirety of the erosive flow took place over approximately 19 min, as each flow velocity interval also included a 15–20 s adjustment time needed to raise the pump speed. The relatively rapid increase in bed stress ensured that the sediment bed did not experience substantial additional conditioning or notable bedform formation or degradation during the erosive flow. Only the highest flow velocities ($\tau_* = 0.048$ to 0.05) were capable of inducing scour, and this behavior was constrained to the edges of the rotating sediment bed. The sediment transport regime in the flume was limited to bedload; that is, the grains were not observed to travel in suspension. The bed was always reset before any new experiment was conducted; thus, observations of sediment motion were made on a newly prepared and conditioned bed, regardless of turntable orientation. A total of 8 trials were conducted for the 6 experimental cases—control (no conditioning), 0°, 45°, 90°, 135°, and 180° relative to the initial conditioning flow direction.

2.2. Flow Characterization

We characterized the streamwise flow velocity using a Nortek Vectrino Profiler, a type of acoustic Doppler profiling velocimeter (ADV). This ADV profiling instrument was mounted over the sediment bed as shown in Figure 1b. The flow conditions at 10 settings of the variable speed pump were measured in a series of calibration runs (3 runs per pump setting). During these calibration runs, the flume was heavily seeded with neutrally buoyant glass microspheres to better reflect acoustic waves emitted by the instrument. The ADV profiler measured a 3 cm velocity profile above the sediment bed, with a 1 mm vertical resolution; measurements were collected at a rate of 65 Hz and time-averaged over a 10 min period (Figure 2a).

We determined the friction velocity, u_*, by fitting the Law of the Wall to our time-averaged velocity profiles, namely

$$u = \frac{u_*}{\kappa} \ln\left(\frac{z}{z_o}\right) \tag{1}$$

where u is the flow velocity, z is the height above the sediment bed, z_o is the roughness length (also fit to measured velocity profiles), and $\kappa = 0.41$ is the von Karman constant. The ADV was positioned such that $z = 0$ cm at the bed surface, and the Law of the Wall was fit to the logarithmic portion of the velocity profile—approximately 0.5 cm to 2.5 cm (Figure 2a). It was found that the friction velocity increased approximately linearly with pump setting (Figure 2b). From the friction velocity, we can calculate the bed stress, τ_b, and Shields number, τ_*, as given by

$$u_* = \sqrt{\frac{\tau_b}{\rho}} \tag{2}$$

and

$$\tau_* = \frac{\tau_b}{(\rho_s - \rho) g D_{50}} \tag{3}$$

where ρ is the fluid density, ρ_s is the sediment density, g is acceleration due to gravity, and D_{50} is the median grain size of the sediment bed. Since velocity profiles were not directly measured for all flow velocity intervals used in the previously described experimental procedure, we used a linear fit between the percentage of the maximum pump output and the friction velocity (Figure 2b), as well as pump output and bed shear stress (Figure 2c) to define u_*, τ_b, τ_*, and the particle Reynolds number $Re_p = u_* D_{50}/\nu$. Re_p ranged from 6.8−10.6 for our experimental conditions, where the kinematic viscosity of water is approximately $\nu = 10^{-6}\text{m}^2/\text{s}$. Thus, our experiments were conducted in a hydraulically transitional flow.

2.3. Sediment Bed Imaging and Particle Tracking

The bed was imaged using a Flea3 monochrome camera (model FL3-U3-13Y3M-C manufactured by Teledyne FLIR) with an SMC Pentax-M 28 mm f2.8 lens that was mounted above the center of the sediment bed looking vertically down through the boat onto a field of view measuring 10.9 cm × 8.75 cm (Figure 1c). During experiments, the sediment bed was illuminated by an ultraviolet light in a dark room, such that the painted sand grains glowed orange; this setup allowed for individual sand grains to be identified and tracked over the course of the video (Kelley et al., 2023). The camera lens was fitted with an optical band pass filter to collect light emitted by the fluorescent paint; thus, these grains appeared bright on the dark background of unpainted sand (Figure 3). Images measuring 1280 × 1024 pixels with a spatial resolution of 0.085 mm per pixel were captured at 120 fps.

We reconstructed the particle trajectories of the fluorescing grains using a multiframe predictive particle-tracking algorithm (Ouellette et al., 2006); grain velocities were then computed from these trajectories via convolution with a smoothing and differentiating kernel (Mordant et al., 2004). Particle tracking has been used to characterize grain behavior in other sediment transport studies (e.g., Lajeunesse et al., 2010; Radice et al., 2017; Salevan et al., 2017; Shim & Duan, 2017), including those investigating stress history effects (Galanis et al., 2022). Parameters specified for the tracking algorithm of Ouellette et al. (2006) included a threshold intensity such that approximately 800 grains were identified in each frame, as well as a minimum and maximum particle area corresponding to the smallest and largest grain sizes. While this algorithm kinematically predicts particle trajectories over multiple frames, we specify a search radius in the predicted particle position if the tracked grain is not immediately found. A suitable search radius was iteratively selected using manual visual inspection to check for track accuracy (Figure 3). To prevent the connection of false tracks, the search radius was conservatively set for each pump setting. Additionally, the tracking algorithm of Ouellette et al. (2006) breaks tracks when a conflict arises (i.e., more than one identified particle in a predicted likely position); thus, false tracks are highly unlikely to occur. While track breakages do take place, the presence of shorter trajectories does not impact our subsequent analysis of grain motion, since we do not consider metrics from individual tracks and only use instantaneous measurements.

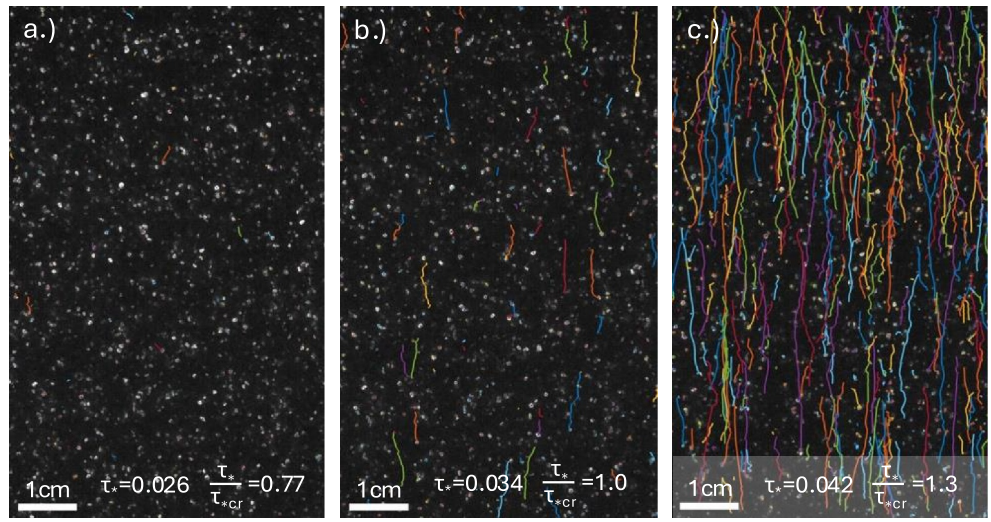

Figure 3. Example sediment tracks from the particle-tracking analysis overlaid onto images of the underlying sediment bed for three flow velocity intervals: (a) the conditioning flow velocity where $\tau_* = 0.026$, (b) the critical flow velocity where $\tau_* = 0.034$, and (c) an above-critical flow velocity where $\tau_* = 0.042$. All tracks longer than 10 frames in a 45 sec movie are shown with individual tracks depicted in various colors. The raw images show fluorescing sand grains over approximately half of the field of view captured by the camera. The flow direction is from the bottom to the top of the images.

We calculate mean grain velocity, $\langle \bar{u}_g \rangle$, by averaging the instantaneous streamwise velocity of each grain identified by the particle-tracking algorithm over all frames of a 45 sec video. The mean grain velocity captures the motions of both grains actively transported through rolls and hops, as well as those that are largely stationary or only jiggling in place. Thus, $\langle \bar{u}_g \rangle$ tends to be much smaller than the typical velocity of a moving grain, as the sediment bed is largely immobile at subcritical conditions. In addition to the grain velocity, we also characterize grain motion by counting the number of active grains in a given frame per unit area, averaged over all frames in a 45 sec video. Termed "grain activity", $\langle \bar{n}_g \rangle$, this metric is similar to the surface density of moving particles introduced by Lajeunesse et al. (2010) or the particle number activity used by Roseberry et al. (2012). A grain is considered active if its instantaneous velocity is above a threshold velocity that varies depending on bulk sediment velocity statistics. The selection of this threshold velocity is discussed further in Section 3.4 below. We can also sum the number of active grains in each frame to determine the total number of active grains over the course of a 45 sec video, ΣN_g. We note that since a particle may be moving across multiple frames, ΣN_g can be larger than the total number of tracked grains. We use overbar notation to indicate a time average and angle brackets to denote a spatial average. Thus, $\langle \bar{u}_g \rangle$, for example, is intended to indicate that grain velocities are averaged over the image area as well as over the duration of the 45 sec video.

3. Results

3.1. Conditioning Flows

During the 20 min conditioning flow, videos of the sediment bed were collected at 5 min intervals. Using this series of videos, we can investigate the grain dynamics during the subcritical conditioning period by measuring the mean grain velocity $\langle \bar{u}_g \rangle$, as well as grain activity $\langle \bar{n}_g \rangle$, and total number of active grains ΣN_g through time. Over the course of this 20 min conditioning flow, we can see that both the mean grain velocity and grain activity decrease, with a substantial reduction in both measurements occurring in the first 5 min followed by a slower leveling-off of grain motions in the second half of the conditioning period (Figure 4). The relationship between the duration of the conditioning flow and the bedload transport rate has previously been characterized using an exponential decay function (Ockelford et al., 2019), which also fits well to the decrease in grain velocity and activity observed during our conditioning flows.

We fit exponential decay functions to the average of four observed conditioning runs and find that the rate constant for the decrease in $\langle \bar{u}_g \rangle$ is $\lambda_{u_g} = 0.18\,[\mathrm{min}^{-1}]$. The rate constant can be used to find the half-life, or in

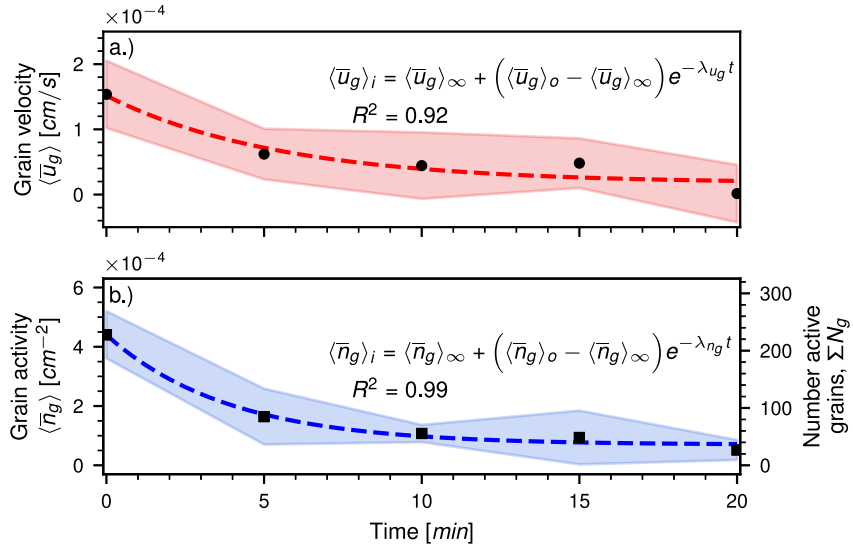

Figure 4. Sediment bed activity over the subcritical conditioning period: (a) mean grain velocity $\langle \bar{u}_g \rangle$ averaged over all identified grains in each video; (b) grain activity $\langle \bar{n}_g \rangle$ (left ordinate axis) and total number of active grains N_g (right ordinate axis) in each video. The form of the exponential decay function and R^2 value is displayed on each panel, with specific equations as follows: (a) $\langle \bar{u}_g \rangle_i = 1.7 \times 10^{-5} + \left(1.5 \times 10^{-4} - 1.7 \times 10^{-5}\right) e^{-0.18t}$; (b) $\langle \bar{n}_g \rangle_i = 6.9 \times 10^{-5} + \left(4.4 \times 10^{-4} - 6.9 \times 10^{-5}\right) e^{-0.26t}$. Shaded regions indicate 95% confidence intervals for both plots; four trials were completed.

this case, the time it takes for the mean grain velocity to reduce by half. This half-life displayed in Figure 4a is 5.5 min. Similarly, the rate constant for decrease in $\langle \bar{n}_g \rangle$ is $\lambda_{n_g} = 0.26 \left[\text{min}^{-1}\right]$. Thus, the half-life, or time it takes for the grain activity to reduce by half, is 3.8 min (Figure 4b). From the half-lives for mean grain velocity and grain activity, we see that the greatest reduction in grain motion occurs during the first few minutes of the conditioning period, which supports our selection of 20 min as the conditioning flow duration. Further, we note that the grain velocity and grain activity measured at the conclusion of the conditioning period correspond to measurements of these parameters for the 0° case at the lowest flow velocity interval in Figures 5a and 9a below.

3.2. Grain Velocities

Using mean grain velocity $\langle \bar{u}_g \rangle$, we can characterize the behavior of the sediment bed during the steps-up in speed of the erosive flow. The data in Figure 5 show the mean grain velocity for each orientation of the sediment bed relative to the flume test section. For all orientations (control, 0°, 45°, 90°, 135°, and 180°), the mean grain velocity becomes higher as the flow speed, and thus the bed stress and Shields stress, increases (Figure 5j).

Once the bed has experienced a subcritical conditioning flow, the mean grain velocity exhibits a dependence on the direction of the subsequent erosive flow. In cases where the conditioning flow and erosive flow occur in the same direction (i.e., 0° offset), we see a reduction in mean grain velocity at Shields stresses up to and including the nominal critical value (Figures 5a and 5c). This reduction in sediment motion due to a history of unidirectional flows agrees with prior studies (e.g., Galanis et al., 2022), although we note that this effect is largely indistinguishable from the unconditioned control case in our experiments once the strength of the erosive flow was increased to stresses above critical (Figures 5d–5i). This pattern is consistent for the case where the erosive flow direction is at an angle of 45° relative to the conditioning flow. The mean grain velocity of the 45° offset is lower than the unconditioned control case, but higher than the unidirectional case (0° offset) for shear stresses up to critical (Figures 5a and 5b). However, the mean grain velocity of the 45° offset is otherwise comparable to the unconditioned control case for the critical and higher Shields stresses (Figures 5c–5i).

The inverse trend occurs for flows that advance from the reversed (180° offset) or nearly reversed (135° offset) direction relative to the conditioning flow. In these cases with flow reversals (both 180° and 135°), the mean grain velocity is higher than the unconditioned control case for all Shields stress increments used in the erosive flow. This behavior is consistent with prior experiments that observed weakening when granular beds are exposed to an

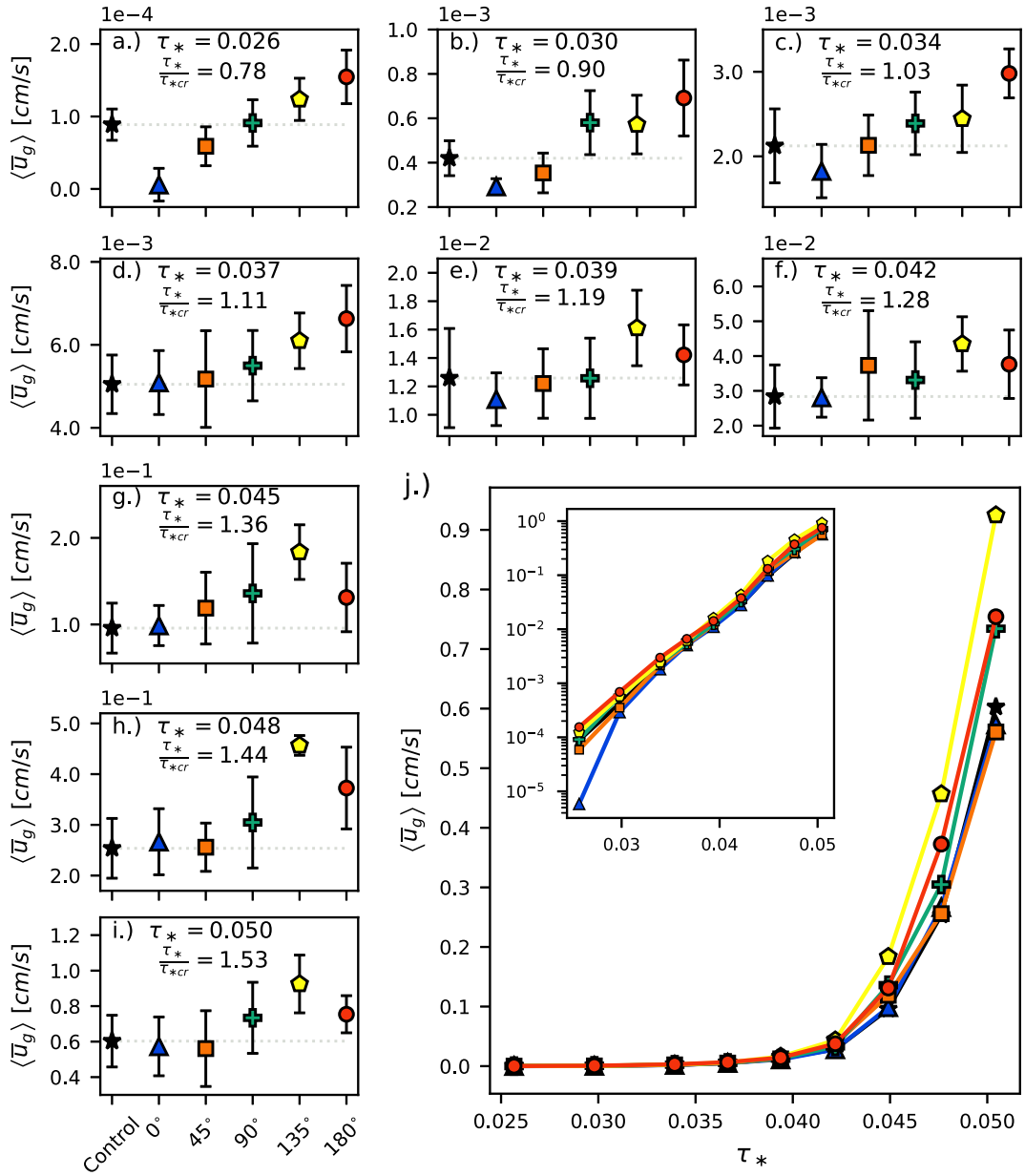

Figure 5. Mean grain velocity averaged over all identified grains in each video $\langle \bar{u}_g \rangle$ for each orientation of the sediment bed, where the angle represents the offset in bed position between the conditioning and erosive flows. Each panel (a–i) shows $\langle \bar{u}_g \rangle$ at increasing steps-up in flow speed and Shields stress, with τ_* and τ_*/τ_{*cr} reported. Error bars indicate the 95% confidence interval computed over eight trials. The faint horizontal gray dotted line is drawn at the $\langle \bar{u}_g \rangle$ of the unconditioned control case and is intended to assist with visual comparison of the $\langle \bar{u}_g \rangle$ of the different bed orientations to the control. Panel (j) shows the mean $\langle \bar{u}_g \rangle$ of eight trials as a function of τ_* for all sediment bed orientations; the inset shows the same data plotted on semi-logarithmic axes.

above-critical flow from a reversed direction (Cúñez et al., 2022; Galanis et al., 2022). We note that when the erosive flow advances from 135° to the conditioning flow, the bed appears weaker with higher mean grain velocities than the full 180° reversal case for Shields stresses above $\tau_* \geq 0.039$ (Figures 5e–5i).

Lastly, for erosive flow directions that are perpendicular to the conditioning flow (90° offset), we observe mean grain velocities that are generally similar to, or slightly higher than, the unconditioned control case. These higher grain velocities tend to occur once the Shields stress has reached $\tau_* \geq 0.045$ (Figures 5g and 5i). Additionally, for

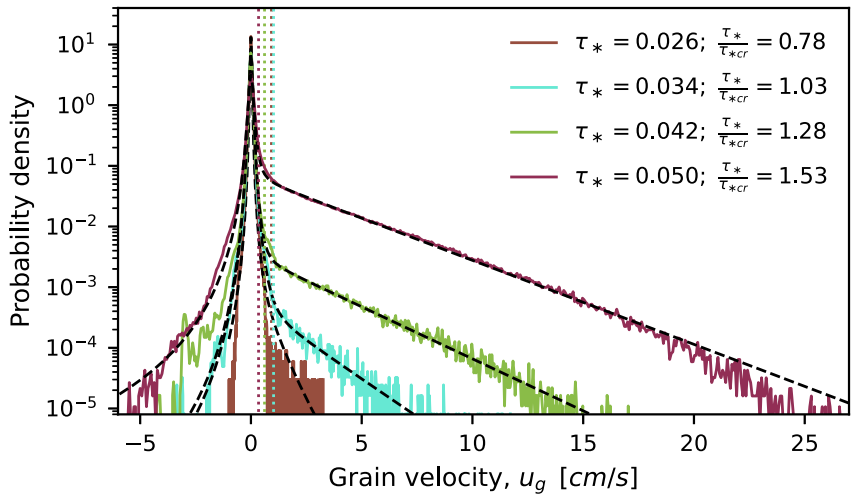

Figure 6. Grain velocity PDFs, $P(u_g)$, measured at four flow velocity intervals for an example unconditioned control case (solid curves). Black dashed curves are fits to the mixture model in Equation 4. The vertical dotted lines indicate the threshold velocities used to determine whether a grain should be considered active for each velocity interval. This method is discussed further in Section 3.4; for reference, the threshold velocities are $u_g = 0.93$ cm/s, $u_g = 1.0$ cm/s, $u_g = 0.61$ cm/s, and $u_g = 0.34$ cm/s for the increasing Shields stresses listed in the figure legend.

these higher bed stresses, we note that the 95% confidence interval of the perpendicular case tends to be greater than the control, indicating that the mean grain velocity experiences greater variability at these conditions.

3.3. How Fast Versus How Many?

Mean grain velocity $\langle \bar{u}_g \rangle$ is a bulk statistic describing the behavior of all identified grains—those that are largely immobile or jiggling in place, as well as grains actively transported as bedload—over each frame of a 45sec video of the sand bed. Thus, as the fluid shear is raised from below-threshold conditions to the onset of motion, it is difficult to determine whether increases in this *average* grain velocity are due to more grains being entrained, these entrained grains having higher velocities, or both. To disentangle these phenomena, we can turn to the full probability density function (PDF) of instantaneous streamwise grain velocities measured for all identified grains in each frame of our videos.

These grain velocity PDFs in Figure 6 show a peak at $u_g = 0$ cm/s with increasingly heavy tails for larger Shields stresses. The cluster of instantaneous velocity measurements around $u_g = 0$ cm/s are due to grains that are mostly immobile but jiggling slightly about their stable locations, especially at or below the onset of motion. This distribution of motions tends to be strongly peaked and symmetric around $u_g = 0$ cm/s, as fluctuations in the flow drive jiggling motions, but not sustained downstream transport. As the fluid stress applied to the sediment bed increases, more and more grains begin to be entrained and transported downstream. The stochastic and independent mobilization of individual grains into active bedload is reflected in the exponential tail of the PDF (Furbish & Schmeeckle, 2013; Roseberry et al., 2012). To account for both grain motions at and just above the onset of motion, we describe the full PDF with a mixture model that incorporates a Student's t-distribution fit to the inner core and an exponential distribution fit to the heavier-than-Gaussian tails (Salevan et al., 2017).

This mixture model is given by

$$P(u_g) = A\frac{\Gamma\left(\frac{\zeta+1}{2}\right)}{\sigma\sqrt{\zeta\pi}\,\Gamma\left(\frac{\zeta}{2}\right)}\left[\frac{\zeta + \left(\frac{u_g}{\sigma}\right)^2}{\zeta}\right]^{\left(\frac{\zeta+1}{2}\right)} + BH(u_g)\,\frac{1}{u_g^*}e^{\left(\frac{u_g}{u_g^*}\right)}, \tag{4}$$

where A is the relative weight of the t-distribution core; B is the relative weight of the exponential tail (where $A + B = 1$); σ indicates the characteristic width of the t-distribution and is related to the magnitude of grain velocity fluctuations; ζ is the heaviness of the t-distribution tails; and u_g^* is a characteristic velocity associated with

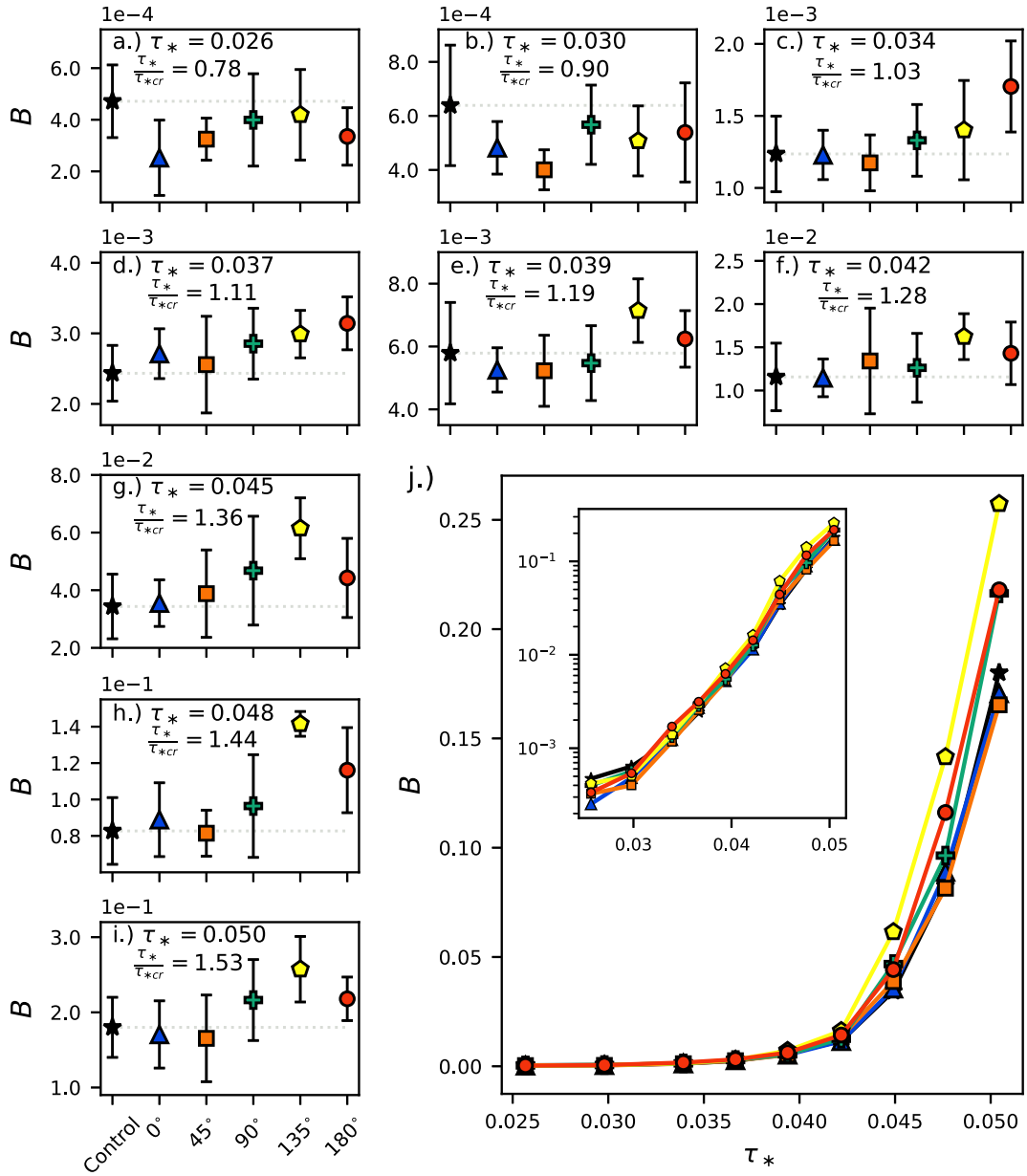

Figure 7. The relative fraction of mobilized grains, B, for each offset angle between the conditioning and erosive flows. Each panel (a–i) shows B at increasing steps-up in fluid shear and Shields stress, with τ_* and τ_*/τ_{*cr} reported. Error bars indicate the 95% confidence interval calculated over eight trials. The faint horizontal gray dotted line is drawn at B of the unconditioned control case and is intended to assist with visual comparison of B for the different bed orientations to the control. Panel (j) shows B with increasing τ_* for all sediment bed orientations; the inset shows the same data plotted on semi-logarithmic axes.

the mobilized grains. We note that when ζ is small, the tails are heavier than a Gaussian with the same variance; when $\zeta \to \infty$, the t-distribution approaches a Gaussian with standard deviation σ. Additionally, Γ is the gamma function and H is the Heaviside function (so that the exponential component of the mixture model is only present for positive grain velocities). We fit this model to our grain velocity PDFs using a standard nonlinear least-squares algorithm.

We focus on the parameters B and u_g^*, which provide information on the grains mobilized as bedload; the parameters σ and ζ are indicative of grain jiggling. B represents the relative quantity of grains mobilized in bedload transport. The data in Figure 7 show B for each orientation of the sediment bed relative to the flume. We observe

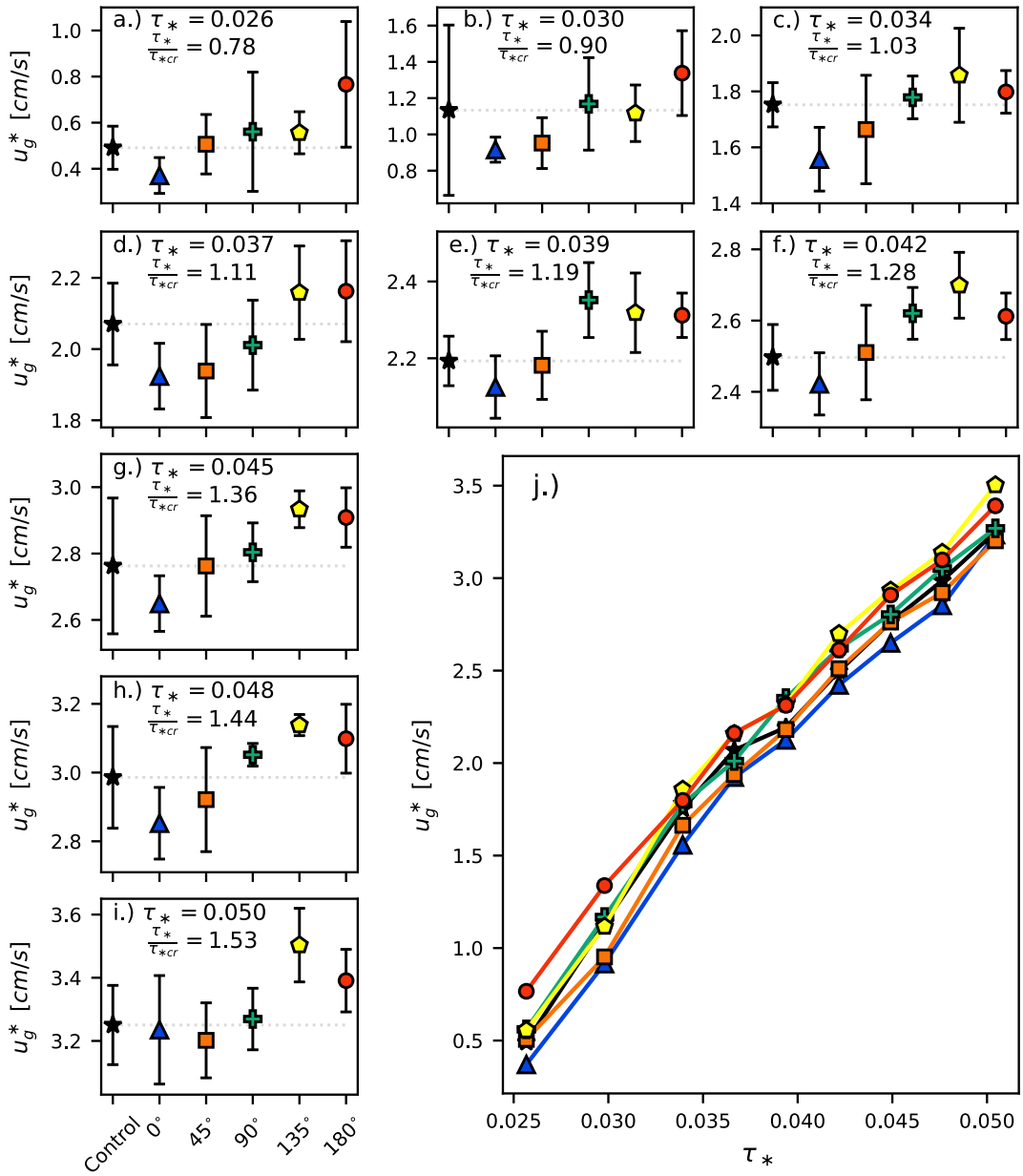

Figure 8. The characteristic bedload velocity, u_g^*, for each offset angle between the conditioning and erosive flows. Each panel (a–i) shows u_g^* at increasing steps-up in fluid shear and Shields stress, with τ_* and τ_*/τ_{*cr} reported. Error bars indicate the 95% confidence interval calculated over eight trials. The faint horizontal gray dotted line is drawn at u_g^* of the unconditioned control case and is intended to assist with visual comparison of u_g^* for the different bed orientations to the control. Panel (j) shows the mean u_g^* with increasing τ_* for all sediment bed orientations. We note that values of u_g^* tend to be unreliable below the onset of motion (Salevan et al., 2017).

that as bed stress increases, the fraction of mobilized grains increases as well; this trend is observed for all orientations (control, 0°, 45°, 90°, 135°, 180°) as seen in Figure 7j.

The fraction of mobilized grains for each orientation generally displays a similar pattern to the behavior of the mean grain velocity $\langle \tilde{u}_g \rangle$ (Figure 5). Compared to the unconditioned control case, we observe a lower B for the 0° and 45° cases below the nominal critical Shields stress (Figures 7a and 7b), a higher B for the 135° and 180° cases at the critical and higher flow velocity intervals (Figures 7c–7i), and a comparable B for the 90° case. These findings are consistent with the change in grain activity observed over the conditioning period (Figure 4b). The 0°

and 45° cases have a lower B since they have already experienced a reduction in the number of active grains, while the 90°, 135°, and 180° cases are freshly exposed to sub-threshold flows from a sufficiently offset direction. This difference may explain why B for the 135° and 180° cases is similar to or slightly lower than the unconditioned control case for flow velocity intervals below critical (Figures 7a and 7b). Lastly, similar to the behavior of the mean grain velocity $\langle \bar{u}_g \rangle$, we note that when the erosive flow advances from 135° relative to the conditioning flow, the bed appears weaker with higher B than the full 180° reversal case for Shields stresses above $\tau_* \geq 0.039$ (Figures 7e–7i).

Meanwhile, u_g^* is a scale parameter with units of velocity and represents the characteristic velocity of the *mobilized* grains. While the values reported as u_g^* are not the directly measured velocities of any physical grains, the mean of an exponential distribution is given by its scale parameter; thus we use u_g^* as a representative bedload velocity. The data in Figure 8 show u_g^* for each orientation of the sediment bed within the flume test section. We observe that as bed stress increases, the characteristic bedload velocity increases as well for all orientations (control, 0°, 45°, 90°, 135°, and 180°) as seen in Figure 8j. u_g^* generally displays a pattern similar to the behavior of the mean grain velocity $\langle \bar{u}_g \rangle$ (Figure 5). The unidirectional stress history case (0° offset) exhibits a lower u_g^* than the unconditioned control case for fluid stresses up to $\tau_* < 0.05$ (Figures 8a–8h). The 45° and 90° flow directions have u_g^* comparable to the unconditioned case, while the reversed (180° offset) and nearly reversed (135° offset) flow directions are faster than the unconditioned control case for almost all fluid stresses. Interestingly, u_g^* is the parameter that most clearly exhibits a persistent directional dependence on the conditioning flow direction even above the onset of motion, with strengthening under the unidirectional conditioning flow (0° offset) and a weakening when conditioning and erosive flows are reversed (180° offset) or nearly reversed (135° offset).

3.4. Grain Activity

To quantify grain activity, we can simply count the number of active grains in a given frame per unit area as described in Section 2.3. While an "active" grain is typically understood to be one rolling, sliding, or hopping as bedload, a quantitative criterion for classifying a grain as active can be difficult to define. Many studies have taken the approach of first choosing a velocity threshold to identify grains that are in motion (González et al., 2017; Roseberry et al., 2012). The selection of this velocity threshold, however, can appear arbitrary and impacts subsequent analysis (Salevan et al., 2017); further, the magnitude of the selected velocity threshold may neglect states of grain activity like jiggling, where grains move in place without significant forward motion (Rebai et al., 2024). Since we are primarily interested in grains moving as bedload, we defined this threshold velocity for grain activity as the grain velocity where the relative contribution of the Student's t-distribution and exponential distribution are equal. This threshold velocity was calculated by identifying the intersection between the Student's t-distribution with parameters A, ζ, and σ and exponential distribution with parameters B and u_g^*, as determined by fitting to the mixture model in Equation 4. Thus, the threshold velocity for grain activity that we choose represents the transition from predominantly motionless or jiggling grain behavior to predominantly bedload, making grain activity $\langle \bar{n}_g \rangle$ a parameter describing the quantity of entrained grains. The threshold velocity for grain activity is shown in Figure 6. We note that as Shields stress increases and the exponential tails of the grain velocity PDFs become increasingly prominent, the threshold velocity for grain activity decreases.

The data in Figure 9 show the grain activity $\langle \bar{n}_g \rangle$ for each orientation of the sediment bed. For all orientations, more grains are entrained as bed stress increases (Figure 9j). Compared to the unconditioned control case, we observe lower grain activity for the 0° and 45° cases below the nominal critical Shields stress (Figures 9a and 9b), which aligns with the reduction in grain activity observed during the conditioning period (Figure 4a). Grain activity is typically higher for the 135° and 180° cases for all Shields stress increments. Grain activity for the 90° case is generally comparable to the unconditioned control. These results for grain activity reflect observations of B, which represents the relative proportion of grains moving as bedload (Figure 7). Since both B and $\langle \bar{n}_g \rangle$ reflect the quantity of mobile grains, we compared these parameters and observed that they are related (Figure 10).

3.5. Grain Activity-Based Threshold of Motion

While grain activity $\langle \bar{n}_g \rangle$ is a useful metric for describing the quantity of mobile grains per unit area averaged over a video, we can further analyze bed behavior by treating each frame as an instantaneous sample of the number of

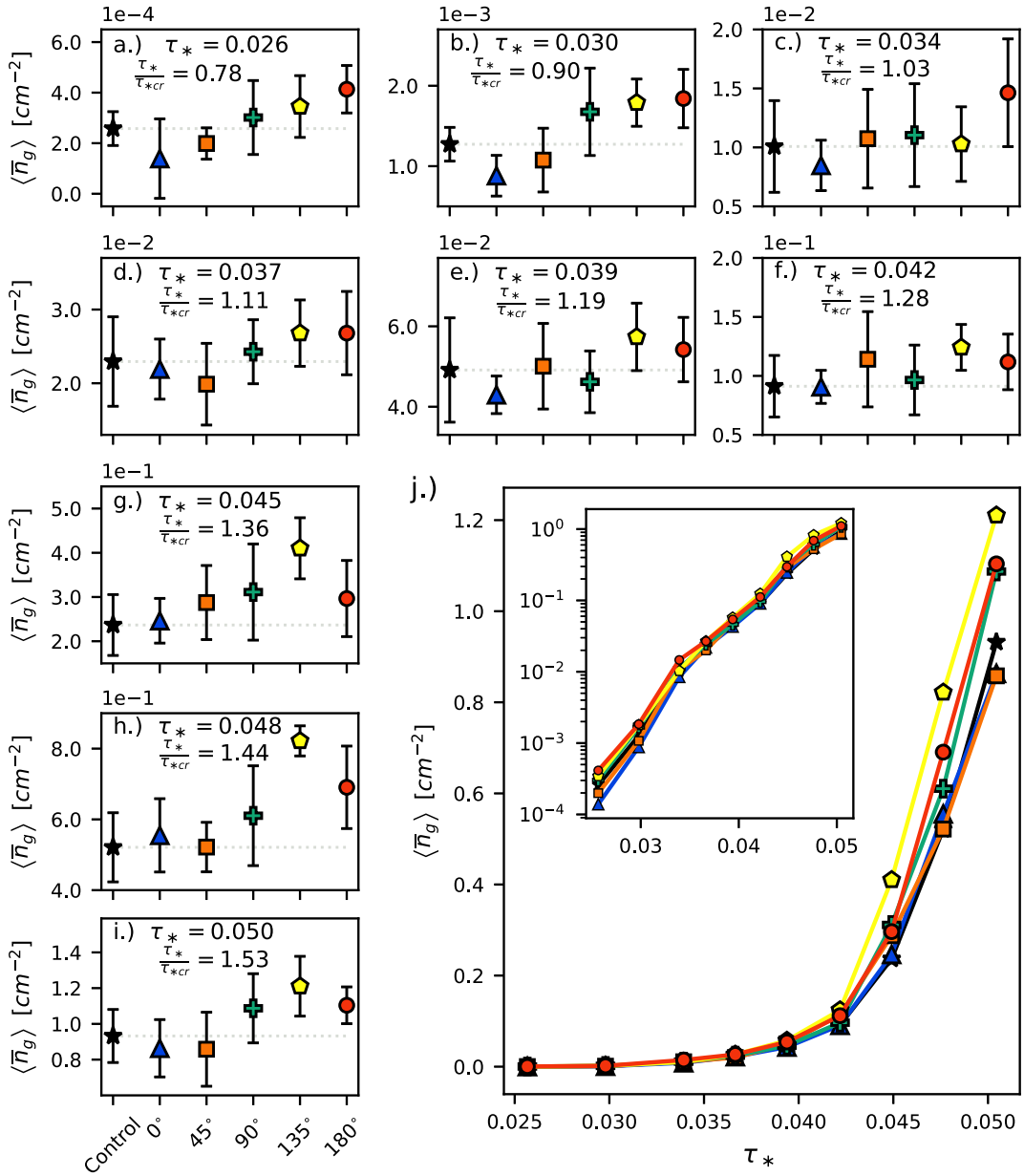

Figure 9. Grain activity, $\langle \bar{n}_g \rangle$, for each orientation of the sediment bed, where the angle represents the offset in bed position between the conditioning and erosive flows. Each panel (a–i) represents $\langle \bar{n}_g \rangle$ at increasing steps-up in flow speed and Shields stress, with τ_* and τ_*/τ_{*cr} reported. Error bars indicate the 95% confidence interval computed over eight trials. The faint horizontal gray dotted line is drawn at $\langle \bar{n}_g \rangle$ of the unconditioned control case and is intended to assist with visual comparison of $\langle \bar{n}_g \rangle$ for the different bed orientations to the control. Panel (j) shows the mean $\langle \bar{n}_g \rangle$ with increasing τ_* for all sediment bed orientations; the inset shows the same data plotted on semi-logarithmic axes.

active grains, N_g. Thus, over an entire video, we can generate a PDF of the number of instantaneously active grains (Figure 11). While some studies fit a negative binomial distribution to the PDF of N_g (Ancey et al., 2006), we follow the methodology of González et al. (2017), who fit the Gamma distribution to their PDF of active grains, defined as

$$P(N_g) = \frac{1}{\theta^k \Gamma(k)} N_g^{k-1} e^{-\frac{N_g}{\theta}}, \tag{5}$$

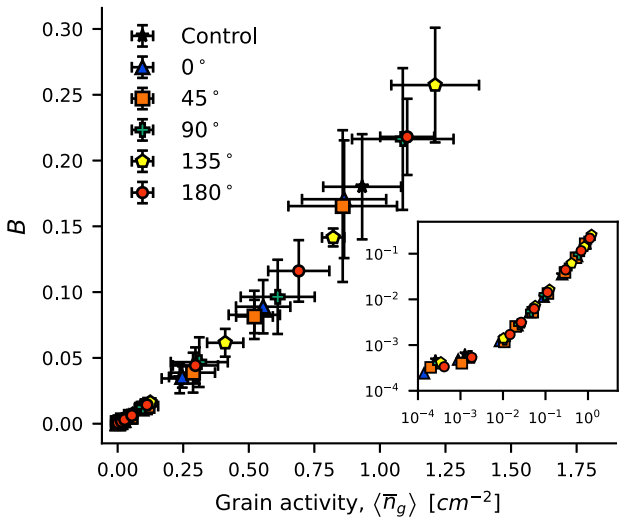

Figure 10. The grain activity for all sediment bed orientations at all Shields stress increments plotted against the B parameter from Equation 4. The error bars represent the 95% confidence interval for both parameters. The inset shows the same data plotted on logarithmic axes.

where k is a shape parameter and θ is a scale parameter. The mean number of active grains is thus given by $\overline{N}_g = k\theta$ and standard deviation is $std(N_g) = \theta\sqrt{k}$.

The reason for selecting the continuous Gamma distribution instead of its discrete counterpart (i.e., the negative binomial distribution) is as follows. When $k < 1$, the Gamma distribution exhibits exponential behavior, which we can see for lower Shields stresses at or below the threshold of motion; in this regime there is a high likelihood that no grains are mobile in any given frame (Figures 11a and 11b). When $k > 1$, the Gamma distribution shifts to behavior that qualitatively appears more log-normal, when a non-zero number of grains are likely to be mobile in a given frame, which occurs at higher Shields stresses (Figures 11c and 11d). This shift in behavior of the Gamma function at $k = 1$ represents a transition in the behavior of the sediment bed from a state of strong intermittency where the most likely observation is of no motion (i.e., $k < 1$) to a regime where the most likely observation is that some grains are in motion (i.e., $k > 1$).

For the various experimental runs, we find the shape parameter k of the best-fit Gamma distribution for the active grains in each video as shear stress is increased from below to above the onset of grain motion. We can then compute an exponential best fit and interpolate the Shields stress where $k = 1$. Although the Shields stress $\tau_{*(k=1)}$ of this transition in bed behavior

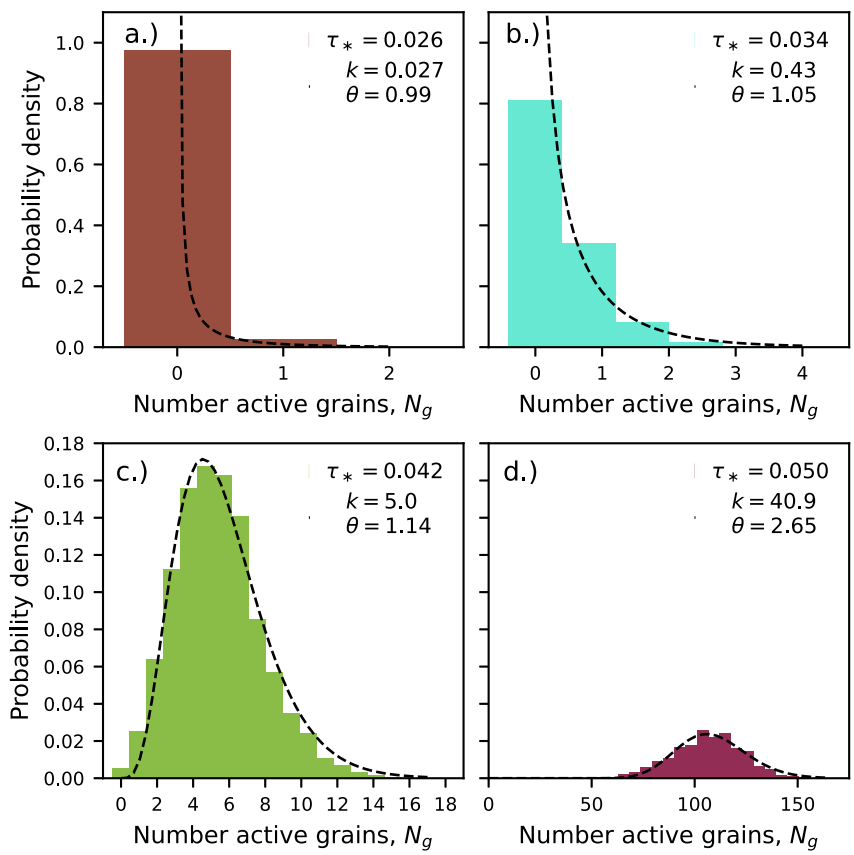

Figure 11. PDFs of the number of active grains in each frame of a video of the sediment bed for an example unconditioned control case; each panel (a–d) depicts bed activity at four flow velocity intervals with τ_* reported. Dashed lines are best fits of these PDFs to a Gamma distribution (Equation 5).

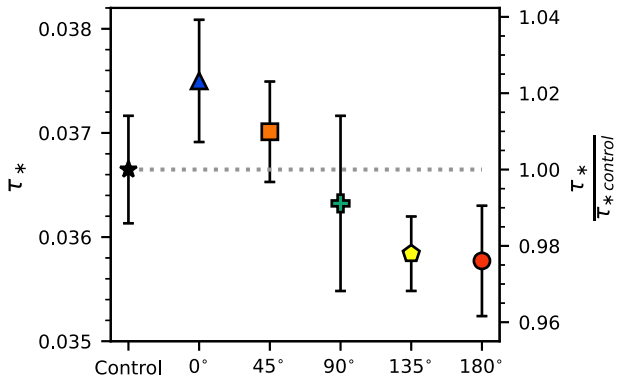

Figure 12. Shields stress $\tau_{*(k=1)}$ at the transition in Gamma distribution behavior for bed mobility. Error bars indicate the 95% confidence interval over 8 trials. The right ordinate axis represents $\tau_{*(k=1)}$ normalized by $\tau_{*(k=1)}$ for the unconditioned control case, with the gray dotted line intended to assist with visual comparison.

does not necessarily represent the threshold of motion, we find that $\tau_{*(k=1)} = 0.037$ is similar to the nominal critical Shields stress ($\tau_{*cr} = 0.033$) for the unconditioned sediment bed. Further, $\tau_{*(k=1)}$ gives a single Shields stress value that can be quantitatively determined and readily compared amongst the experimental cases, while τ_{*cr} can be more challenging to identify (e.g., Lavelle & Mofjeld, 1987; Salevan et al., 2017). When we compare $\tau_{*(k=1)}$ across the five orientations of the sediment bed within the flume, we observe a clear (albeit small) angular dependence (Figure 12). There is a 2.3% increase in $\tau_{*(k=1)}$ for the unidirectional case (0° offset) and a 2.4% decrease for the reversed case (180° offset) when compared to the unconditioned control. This observation confirms the trend shown in the previously described measurements of mean grain velocity $\langle \bar{u}_g \rangle$ and calculated parameters describing the characteristic bedload velocity u_g^* and grain activity $\langle \bar{n}_g \rangle$, with the greatest strengthening occurring when the conditioning and erosive flow are aligned (0° offset) and the greatest weakening when the conditioning and erosive flow are reversed (180° offset). Further, we see that the 90° case, where the erosive flow advances from a perpendicular direction to the conditioning flow, is similar to the unconditioned control but demonstrates greater variability.

We can also perform an analogous analysis to identify the critical Shields stress of each sediment bed orientation using the so-called Yalin criterion (Neill & Yalin, 1969), a visual method for defining τ_{*cr} by counting the number of grain detachments observed over a given area, α, and time, t and comparing it to the value

$$N_{Yalin} = \varepsilon \alpha t \left[\frac{\rho D_{50}}{(\rho_s - \rho) g} \right]^{-\frac{1}{2}} \tag{6}$$

where α corresponds to the bed area in the camera field of view ($95.4\ \text{cm}^2$), t is the duration of a video of grain motions (45 sec), and ε is a lower limit for threshold detection, set at $\varepsilon = 1 \times 10^{-6}$ by Neill and Yalin (1969). This method has been used to define τ_{*cr} in other stress history studies (Ockelford et al., 2019; Paphitis & Collins, 2005). For the various experimental runs, we can count the total number of active grains in each video ΣN_g and plot this value as a function of τ_*. By fitting an exponential function to each run, we can then find τ_{*cr} by interpolating the Shields stress where $\Sigma N_g = N_{Yalin}$, which for our case is 317 total active grains identified over the course of a video. This analysis shows that there is a 6.8% increase in τ_{*cr} for the 0° case compared to the unconditioned control, and a 4.5% decrease for the 180° case. The general trend of decreasing τ_{*cr} with increasing angular offset between the conditioning and erosive flows persists, similar to Figure 12. We note that Paphitis and Collins (2005), who like us used a narrow grain size distribution of natural sand placed within an inset sediment bed of similar dimensions, observed an increase in critical Shields stress ranging from approximately 5%–10% in their experimental cases where a 0.387 mm and a 0.774 mm sand bed were subjected to a 20 min conditioning flow at 77%–83% of the critical Shields stress.

4. Discussion

The data we collect show that bed erodibility is dependent on directional flow (and therefore stress) history, suggesting that the mechanisms for storing memory in the granular bed must have an anisotropic component. Previous experiments have typically attributed the development of memory stress to smoothing of the bed surface due to compaction and relocation and reorientation of protruding grains (Masteller & Finnegan, 2017; Ockelford & Haynes, 2013), in addition to an increase in the packing fraction within the bed subsurface (Allen & Kudrolli, 2018). These mechanisms, however, would be isotropic, and so cannot fully explain our results. The anisotropic component is likely attributable—at least in part—to direction-dependent strain hardening that results in a fragile or shear jammed state (Bi et al., 2011; Cates et al., 1998). Cúñez et al. (2022), who recently conducted stress history experiments using both reversed and oscillating flows, identified both compaction and shear jamming as mechanisms for memory storage. When our conditioned sand bed is exposed to fluid shear from an

opposing or near-opposing direction (180° and 135° offsets), the preferentially loaded contact networks between grains are more susceptible to disruption leading to erosion at a lower Shields stress. However, we acknowledge that our experiments only observe the surface of the sediment bed; thus, we cannot distinguish whether the source of the anisotropy we observed is due to subsurface phenomena, such as shear jamming and the formation of force chains through preferential loading of grain contacts, or a surface phenomenon where grains are wedged into pockets that are preferentially supported from only certain directions. Despite this inability to peer within the bed subsurface, we identify two observations that support the presence of shear jamming as a mechanism for memory stress storage: (a) the persistence of stress history effects above τ_{*cr} in beds sheared by reversed flows, but not unidirectional flows; and (b) signals of stress history appearing in both the quantity of mobilized grains as well as their characteristic grain velocity.

4.1. The Persistence of Memory Stress

Although the data we collected show that bed erodibility is dependent on directional flow (and therefore stress) history, we find that the signal of this history in our sediment bed only persists above τ_{*cr} for cases with flow reversals (180° offset) or near-reversals (135° offset). Evidence of bed strengthening under unidirectional flows, however, does not persist at higher flow velocities. In our experiments, this strengthening effect is most pronounced in the 0° case (and the 45° case to a lesser extent) for Shields stresses at and below the nominal critical value. We can confirm that the bed is indeed becoming less mobile by examining the reduction in mean grain velocity $\langle \bar{u}_g \rangle$ and grain activity $\langle \bar{n}_g \rangle$ over the 20 min conditioning flow (Figure 4). However, as the flow velocity begins to exceed the critical value for sediment motion, the bed behavior approaches that of the unconditioned control case for mean grain velocity $\langle \bar{u}_g \rangle$, B, and grain activity $\langle \bar{n}_g \rangle$. This "erasure" of memory stress is consistent with observations of natural gravel-bed rivers. Bed stability increases and bedload transport decreases during drier times of year when streamflow is low and bankfull floods are uncommon; subsequently, during spring snowmelt or rainy periods when bankfull or greater floods tend to occur, these rapid flows disrupt any structure or orientation that may have developed and "reset" the bed to a more mobile and unstructured state (Masteller et al., 2019; Oldmeadow & Church, 2006; Vericat et al., 2006). Further, a similar erasure of stress history for $\tau_* \gg \tau_{*cr}$ has been observed in flume studies using both graded gravel bed material (An et al., 2021), as well as monodisperse beads sheared by a laminar flows (Cúñez et al., 2022).

Bed weakening when exposed to reversed fluid shear, while less studied, has also previously been observed by Galanis et al. (2022) and Cúñez et al. (2022). Interestingly, the signal of weakening in beds conditioned by these reversed flows (180° and 135° offsets) is much more evident for flows above critical in our experiments. The question then arises as to why the signal of bed weakening persists above the critical Shields stress—after all, the same magnitude and duration were used for all conditioning flows, as were the same flow velocity intervals in the erosive flow.

We explain this dichotomy as follows: when the sediment bed is sheared by the sub-threshold conditioning flow, creep occurs at both the bed surface and subsurface, decaying exponentially with depth (Allen & Kudrolli, 2018; Houssais et al., 2015). When sheared by the erosive flow $\tau_* > \tau_{*cr}$ in the unidirectional case (0°, and slightly offset 45° case), the bed surface is mobilized as bedload; however, the bed subsurface continues to creep and undergo shear strengthening. Experiments conducted by Cúñez et al. (2022) demonstrate a distinct transition between the subsurface creeping and active bedload layers in granular materials repeatedly subjected to unidirectional fluid shear, with strain hardening continuing to occur for flows up to $4\tau_{*cr}$ (after which point enough of the sediment bed is fluidized so as to erase stress history). Thus, we suspect that in our unidirectional case (0° and 45° offsets), the upper bedload layer has achieved similar bed mobility statistics as the unconditioned control, especially since the highest flow velocity interval we tested was approximately $1.5\tau_{*cr}$. In the cases where the direction of the erosive flow is reversed or nearly reversed (180° and 135° offsets), the sand bed likely developed a wider shear zone, thus experiencing greater disruption of grain contacts and increased sediment motion further into the subsurface (Slotterback et al., 2012; Toiya et al., 2004). We hypothesize that evidence of this deeper disruption manifests as increased grain mobility when $\tau_* > \tau_{*cr}$ during the reversed flow conditions. However, if bed strengthening and weakening were due to surface-only effects (e.g., anisotropically oriented grain pockets), we would expect that the 180° and 135° cases would exhibit grain motion statistics approaching that of the unconditioned control for $\tau_* > \tau_{*cr}$, similar to the 0° and 45° cases.

It is also possible that this effect is due to the method we used to smooth and prepare the bed, although this rationale does not negate the role that subsurface grain re-arrangement may have played. As described above, before each experimental run, we stirred the sand bed and then dragged a mesh screen across the bed surface—always in the downstream direction of the conditioning flow. The shear imparted by dragging the screen, similar to fluid shear, may also have imparted a stress history that contributed to bed strengthening and promoted erosion when the orientation of the sediment bed was reversed. Interestingly, for nearly all metrics, the 135° case appears weaker than the 180° case, exhibiting the greatest grain activity and grain velocity. It is unclear why the 135° orientation is consistently more erodible; a possibility is that the shear imparted onto the sediment bed from the bed leveling procedure produced a downstream-oriented directional fabric that persisted through the 180° flow reversal, resulting in a slightly stronger 180° case compared to the 135° case. Another possibility is the ability of grains to more easily move around others that have been strengthened by the conditioning flow when the erosive flow is not completely reversed, but more research is required to explain this observation definitively.

4.2. Signals of Stress History: Grain Velocity Versus Activity

An additional observation that requires further explanation is the signal of bed strengthening and weakening that appears in both the quantity of grains that are mobilized, as measured by the parameter B (Figure 7) and grain activity $\langle \bar{n}_g \rangle$ (Figure 9), and the velocity of the mobilized grains, as quantified through the characteristic bedload velocity u_g^* (Figure 8). Given that conditioning flows are capable of modifying the configuration of grains both on the bed surface and within the subsurface, we would expect that the number of active grains varies as a function of directional stress history. The characteristic bedload velocity u_g^* also varies as a function of directional stress history; however, this observation is more difficult to explain as we expect the typical velocity of moving grains to scale with fluid shear (e.g., Shim & Duan, 2019), which is kept constant across experimental runs.

As previously mentioned, u_g^* is a scale parameter derived from the exponential component of the mixture model fit to a PDF of instantaneous grain velocities (Equation 4). The exponential tail is representative of grains actively mobilized by the overlying fluid and becomes more pronounced for flow velocities above τ_{*cr} (Figure 6). While we use the terminology "characteristic bedload velocity" for u_g^*, it is formally a statistical parameter that is a property of the ensemble of moving grains rather than the velocity of any individual moving grain. In the experimental cases with flow reversals (180° and 135° offsets), deeper grain motion within a wider shear zone may result in collective grain entrainment and sustained sediment transport supported through inertial interactions (Clark et al., 2015). Alternatively, when the sand bed is conditioned by unidirectional flows (0° offset), sand grains may experience fewer collective entrainment events and dislodged grains may lose momentum to a more jammed and static sediment bed. The flight of individual sand grains across the bed surface may then still scale with the overlying fluid shear; however, when we consider the ensemble of these mobilized sediment grains, the aggregate grain behaviors (i.e., starting and stopping vs. sustained motion) and their dependence on prior flow direction may then be contained in the characteristic bedload velocity u_g^*.

In addition to the ensemble of grain-scale motions at and below the surface of the sand bed, sediment velocity dynamics are also controlled by complex interactions between the overlying flow field and sediment bed configuration (e.g., Escauriaza et al., 2023; Papanicolaou et al., 2001). Although the large-scale flow velocity conditions were kept constant across the experimental runs, the fluid flow field near the sediment bed may also vary in response to directional flow history. Experiments by Cooper et al. (2008) show that near-bed flow velocity and turbulence statistics vary between a gravel bed conditioned by unidirectional flows and one exposed to a conditioning flow that was subsequently rotated by 90°. The 90°-rotated bed was observed to be hydraulically rougher with a slower near-bed velocity profile. While it is difficult to directly apply observations from a graded gravel bed our uniform sand bed, we recognize that near-bed flow characteristics may also respond in unexpected ways to the bed surface and subsurface changes that come about from the development of memory stress.

Since we can measure both the number of active grains and a characteristic bedload velocity, a logical follow-up question to this analysis is whether we can cast the sediment transport rate in terms of these quantities we have measured. In steady-state conditions, the sediment transport rate, q_s, can be defined as the product of a mean grain velocity and a grain concentration (Bridge & Dominic, 1984; Lajeunesse et al., 2010; Parker et al., 2003; Seminara et al., 2002; Wiberg & Dungan Smith, 1989; Wong et al., 2007). Using terms we have obtained from our experiments, we can take the mean grain velocity to be the characteristic bedload velocity u_g^*, and can determine

grain concentration using the grain activity $\langle \bar{n}_g \rangle$ and the volume of a typical grain $\sim D^3$. Using these quantities, the bedload transport rate would then be given by

$$q_s = cD^3 u_g^* \langle \bar{n}_g \rangle. \tag{7}$$

Additionally, since we determine grain activity using a population of fluorescent-painted grains and assume that this population accurately reflects the entirety of the bed, we may need to add a correction factor, c, accounting for the ratio of painted to unpainted grains at the surface. Lastly, given appropriate calibration, the parameter B obtained from the best-fit mixture model could potentially be used in place of grain activity. Thus, the bedload transport rate could entirely be calculated based on a statistical characterization using the grain velocity PDF.

5. Conclusion

We conducted experiments using a rotating sediment bed apparatus to develop directional stress history in a granular bed composed of natural sand. The experimental protocol involved conditioning the sediment bed for 20 min at a flow that delivered 80% of the critical shear stress, followed by rotation and exposure to an erosive flow. We find that the onset of motion is influenced by the angular direction of a conditioning flow relative to the bed-mobilizing flow. Strengthening behavior was observed when the conditioning and erosive flows advance from the same or similar direction (i.e., 0° and 45° offsets); however, this behavior is less evident for bed stresses above the nominal critical value. Weakening behavior was observed when the erosive flow advances from a reversed or nearly reversed direction relative to the conditioning flow (i.e., 180° and 135° offsets). The case where the erosive flow advances from the direction perpendicular to the conditioning flow (i.e., 90° offset) exhibits similar behavior to the unconditioned control case, but with greater variability.

These results support the existence of an anisotropic component for the mechanism that stores memory in granular beds. Although we cannot determine whether the memory originates from a surface-level or subsurface mechanism, we argue that sustained weakening observed in the 135° and 180° experimental cases when $\tau_* > \tau_{*cr}$ is evidence of increased grain motion deeper within the bed subsurface. Further, bed strengthening and weakening impacts both the quantity of mobile grains, as well as the velocity of this mobile grain ensemble. Since the characteristic bedload velocity is greater for weaker beds, sediment flux is likely higher in systems with reversals, even if the threshold of motion may not have changed significantly.

Finally, we confirm the value of statistical analyses in evaluating bedload behavior. Using both grain velocity and grain activity PDFs, we are able to extract useful metrics like a characteristic bedload velocity and thresholds for changes in bed behavior that are representative of the onset of motion. These metrics show clear distinctions between our various experimental cases and may be useful when calculating sediment flux.

Conflict of Interest

The authors declare no conflicts of interest relevant to this study.

Data Availability Statement

All relevant data and code used to generate the figures in this paper are deposited in figshare, a free and open repository. These data sets can be accessed using the following link: https://doi.org/10.6084/m9.figshare.28797692.v2 (Bodek et al., 2025).

Acknowledgments
Financial support was provided by the Army Research Office (ARO Award #W911NF-23-1-0032); The authors thank Bill Sabala for his assistance with the design and fabrication of the rotating sediment dish apparatus, M. Colin Marvin and Mathieu Lapotre for assistance with grain size measurements, Stanford Research Computing for computational support through the Sherlock cluster, and Claire Masteller for helpful discussions. The authors also thank three anonymous reviewers whose constructive comments have helped improve this paper.

References

Allen, B., & Kudrolli, A. (2018). Granular bed consolidation, creep, and armoring under subcritical fluid flow. *Physical Review Fluids*, *3*(7), 074305. https://doi.org/10.1103/physrevfluids.3.074305

An, C., Hassan, M. A., Ferrer-Boix, C., & Fu, X. (2021). Effect of stress history on sediment transport and channel adjustment in graded gravel-bed Rivers. *Earth Surface Dynamics*, *9*(2), 333–350. https://doi.org/10.5194/esurf-9-333-2021

Ancey, C., Böhm, T., Jodeau, M., & Frey, P. (2006). Statistical description of sediment transport experiments. *Physical Review E—Statistical Physics, Plasmas, Fluids, and Related Interdisciplinary Topics*, *74*(1), 011302. https://doi.org/10.1103/PhysRevE.74.011302

Ashida, K., & Michiue, M. (1973). Studies on bed-load transport rate in open channel flows. In *Sediment transportation* (Vol. 1).

Behringer, R. P., & Chakraborty, B. (2018). The physics of jamming for granular materials: A review. *Reports on Progress in Physics*, *82*(1), 012601. https://doi.org/10.1088/1361-6633/aadc3c

Bi, D., Zhang, J., Chakraborty, B., & Behringer, R. P. (2011). Jamming by shear. *Nature*, *480*(7377), 355–358. https://doi.org/10.1038/nature10667

Bodek, S., Wang, D., Shattuck, M. D., O'Hern, C. S., & Ouellette, N. T. (2025). Grain velocities from anisotropic stress history experiments [Dataset]. *Figshare*. https://doi.org/10.6084/m9.figshare.28797692.v2

Bridge, J. S., & Dominic, D. F. (1984). Bed load grain velocities and sediment transport rates. *Water Resources Research*, *20*(4), 476–490. https://doi.org/10.1029/WR020i004p00476

Buffington, J. M., & Montgomery, D. R. (1997). A systematic analysis of eight decades of incipient motion studies, with special reference to gravel-bedded rivers. *Water Resources Research*, *33*(8), 1993–2029. https://doi.org/10.1029/96WR03190

Cameron, S. M., Nikora, V. I., & Witz, M. J. (2020). Entrainment of sediment particles by very large-scale motions. *Journal of Fluid Mechanics*, *888*, A7. https://doi.org/10.1017/jfm.2020.24

Cates, M. E., Wittmer, J. P., Bouchaud, J.-P., & Claudin, P. (1998). Jamming, force chains, and fragile matter. *Physical Review Letters*, *81*(9), 1841–1844. https://doi.org/10.1103/PhysRevLett.81.1841

Charru, F., Mouilleron, H., & Eiff, O. (2004). Erosion and deposition of particles on a bed sheared by a viscous flow. *Journal of Fluid Mechanics*, *519*, 55–80. https://doi.org/10.1017/S0022112004001028

Clark, A. H., Shattuck, M. D., Ouellette, N. T., & O'Hern, C. S. (2015). Onset and cessation of motion in hydrodynamically sheared granular beds. *Physical Review E*, *92*(4), 042202. https://doi.org/10.1103/physreve.92.042202

Clark, A. H., Shattuck, M. D., Ouellette, N. T., & O'Hern, C. S. (2017). Role of grain dynamics in determining the onset of sediment transport. *Physical Review Fluids*, *2*(3), 034305. https://doi.org/10.1103/PhysRevFluids.2.034305

Cooper, J., Aberle, J., Koll, K., McLelland, S., Murphy, B., Tait, S., & Marion, A. (2008). Observation of the near-bed flow field over gravel bed surfaces with different roughness length scales. In *Proceedings of the international conference on fluvial hydraulics river flow 2008* (Vol. 3).

Cúñez, F. D., Franklin, E. M., Houssais, M., Arratia, P., & Jerolmack, D. J. (2022). Strain hardening by sediment transport. *Physical Review Research*, *4*(2), L022055. https://doi.org/10.1103/PhysRevResearch.4.L022055

Dey, S. (1999). Sediment threshold. *Applied Mathematical Modelling*, *23*(5), 399–417. https://doi.org/10.1016/S0307-904X(98)10081-1

Diplas, P., Dancey, C. L., Celik, A. O., Valyrakis, M., Greer, K., & Akar, T. (2008). The role of impulse on the initiation of particle movement under turbulent flow conditions. *Science*, *322*(5902), 717–720. https://doi.org/10.1126/science.1158954

Einstein, H. A., & El-Samni, E.-S. A. (1949). Hydrodynamic forces on a rough Wall. *Reviews of Modern Physics*, *21*(3), 520–524. https://doi.org/10.1103/RevModPhys.21.520

Engelund, F., & Fredsøe, J. (1976). A sediment transport model for straight alluvial channels. *Hydrology Research*, *7*(5), 293–306. https://doi.org/10.2166/nh.1976.0019

Escauriaza, C., González, C., Williams, M. E., & Brevis, W. (2023). Models of bed-load transport across scales: Turbulence signature from grain motion to sediment flux. *Stochastic Environmental Research and Risk Assessment*, *37*(3), 1039–1052. https://doi.org/10.1007/s00477-022-02333-9

Furbish, D. J., & Schmeeckle, M. W. (2013). A probabilistic derivation of the exponential-like distribution of bed load particle velocities. *Water Resources Research*, *49*(3), 1537–1551. https://doi.org/10.1002/wrcr.20074

Galanis, M., Shattuck, M. D., O'Hern, C. S., & Ouellette, N. T. (2022). Directional strengthening and weakening in hydrodynamically sheared granular beds. *Physical Review Fluids*, *7*(1), 013802. https://doi.org/10.1103/PhysRevFluids.7.013802

García, M. H. (2013). Sediment transport and morphodynamics. *Sedimentation Engineering*, 21–163. https://doi.org/10.1061/9780784408148.ch02

Gomez, B. (1983). Temporal variations in the particle size distribution of surficial bed material: The effect of progressive bed armouring. *Geografiska Annaler: Series A, Physical Geography*, *65*(3–4), 183–192. https://doi.org/10.1080/04353676.1983.11880085

González, C., Richter, D. H., Bolster, D., Bateman, S., Calantoni, J., & Escauriaza, C. (2017). Characterization of bedload intermittency near the threshold of motion using a Lagrangian sediment transport model. *Environmental Fluid Mechanics*, *17*(1), 111–137. https://doi.org/10.1007/s10652-016-9476-x

Haynes, H., & Pender, G. (2007). Stress history effects on graded bed stability. *Journal of Hydraulic Engineering*, *133*(4), 343–349. https://doi.org/10.1061/(ASCE)0733-9429(2007)133:4(343)

Houssais, M., Ortiz, C. P., Durian, D. J., & Jerolmack, D. J. (2015). Onset of sediment transport is a continuous transition driven by fluid shear and granular creep. *Nature Communications*, *6*(1), 6527. https://doi.org/10.1038/ncomms7527

Kelley, M., Mahon, R. C., Ganti, V., Daas, D., & Leary, K. (2023). *Linking particle trajectories to changes in bedform 3-dimensionality*. AGU Fall Meeting. (Poster EP41D-2341).

Kirchner, J. W., Dietrich, W. E., Iseya, F., & Ikeda, H. (1990). The variability of critical shear stress, friction angle, and grain protrusion in water-worked sediments. *Sedimentology*, *37*(4), 647–672. https://doi.org/10.1111/j.1365-3091.1990.tb00627.x

Lajeunesse, E., Malverti, L., & Charru, F. (2010). Bed load transport in turbulent flow at the grain scale: Experiments and modeling. *Journal of Geophysical Research: Earth Surface*, *115*(F4). https://doi.org/10.1029/2009JF001628

Lavelle, J. W., & Mofjeld, H. O. (1987). Do critical stresses for incipient motion and erosion really exist? *Journal of Hydraulic Engineering*, *113*(3), 370–385. https://doi.org/10.1061/(asce)0733-9429(1987)113:3(370)

Luque, R. F., & Van Beek, R. (1976). Erosion and transport of bed-load sediment. *Journal of Hydraulic Research*, *14*(2), 127–144. https://doi.org/10.1080/00221687609499677

Majmudar, T. S., & Behringer, R. P. (2005). Contact force measurements and stress-induced anisotropy in granular materials. *Nature*, *435*(7045), 1079–1082. https://doi.org/10.1038/nature03805

Mao, L. (2018). The effects of flood history on sediment transport in gravel-bed rivers. *Geomorphology*, *322*, 196–205. https://doi.org/10.1016/j.geomorph.2018.08.046

Mao, L., Dell'Agnese, A., Huincache, C., Penna, D., Engel, M., Niedrist, G., & Comiti, F. (2014). Bedload hysteresis in a glacier-fed mountain river. *Earth Surface Processes and Landforms*, *39*(7), 964–976. https://doi.org/10.1002/esp.3563

Masteller, C. C., & Finnegan, N. J. (2017). Interplay between grain protrusion and sediment entrainment in an experimental flume. *Journal of Geophysical Research: Earth Surface*, *122*(1), 274–289. https://doi.org/10.1002/2016JF003943

Masteller, C. C., Finnegan, N. J., Turowski, J. M., Yager, E. M., & Rickenmann, D. (2019). History-dependent threshold for motion revealed by continuous bedload transport measurements in a steep Mountain stream. *Geophysical Research Letters*, *46*(5), 2583–2591. https://doi.org/10.1029/2018GL081325

Masteller, C. C., Johnson, J. P. L., Rickenmann, D., & Turowski, J. M. (2025). Modeling memory in gravel-bed rivers: A flow-history-dependent relation for evolving thresholds of motion. *Earth Surface Dynamics*, *13*(4), 593–605. https://doi.org/10.5194/esurf-13-593-2025

Meyer-Peter, E., & Müller, R. (1948). Formulas for bed-load transport. In *IAHSR 2nd meeting, stockholm*. appendix 2.

Monteith, H., & Pender, G. (2005). Flume investigations into the influence of shear stress history on a graded sediment bed. *Water Resources Research*, *41*(12). https://doi.org/10.1029/2005WR004297

Mordant, N., Crawford, A. M., & Bodenschatz, E. (2004). Experimental Lagrangian acceleration probability density function measurement. *Physica D*, *193*(1), 245–251. https://doi.org/10.1016/j.physd.2004.01.041

Neill, C. R., & Yalin, M. S. (1969). Quantitative definition of beginning of bed movement. *Journal of the Hydraulics Division*, *95*(1), 585–588. https://doi.org/10.1061/jyceaj.0002022

Ockelford, A., & Haynes, H. (2013). The impact of stress history on bed structure. *Earth Surface Processes and Landforms*, *38*(7), 717–727. https://doi.org/10.1002/esp.3348

Ockelford, A., Woodcock, S., & Haynes, H. (2019). The impact of inter-flood duration on non-cohesive sediment bed stability. *Earth Surface Processes and Landforms*, *44*(14), 2861–2871. https://doi.org/10.1002/esp.4713

Oldmeadow, D. F., & Church, M. (2006). A field experiment on streambed stabilization by gravel structures. *Geomorphology*, *78*(3–4), 335–350. https://doi.org/10.1016/j.geomorph.2006.02.002

O'Riordan, C. A., Monismith, S. G., & Koseff, J. R. (1993). A study of concentration boundary-layer formation over a bed of model bivalves. *Limnology & Oceanography*, *38*(8), 1712–1729. https://doi.org/10.4319/lo.1993.38.8.1712

Ouellette, N. T., Xu, H., & Bodenschatz, E. (2006). A quantitative study of three-dimensional Lagrangian particle tracking algorithms. *Experiments in Fluids*, *40*(2), 301–313. https://doi.org/10.1007/s00348-005-0068-7

Pähtz, T., Clark, A. H., Valyrakis, M., & Durán, O. (2020). The physics of sediment transport initiation, cessation, and entrainment across Aeolian and fluvial environments. *Reviews of Geophysics*, *58*(1), e2019RG000679. https://doi.org/10.1029/2019RG000679

Papanicolaou, A. N., Diplas, P., Dancey, C. L., & Balakrishnan, M. (2001). Surface roughness effects in near-bed turbulence: Implications to sediment entrainment. *Journal of Engineering Mechanics*, *127*(3), 211–218. https://doi.org/10.1061/(ASCE)0733-9399(2001)127:3(211)

Paphitis, D., & Collins, M. B. (2005). Sand grain threshold, in relation to bed "stress history": An experimental study. *Sedimentology*, *52*(4), 827–838. https://doi.org/10.1111/j.1365-3091.2005.00710.x

Parker, G., Seminara, G., & Solari, L. (2003). Bed load at low Shields stress on arbitrarily sloping beds: Alternative entrainment formulation. *Water Resources Research*, *39*(7). https://doi.org/10.1029/2001WR001253

Pretzlav, K. L. G., Johnson, J. P. L., & Bradley, D. N. (2020). Smartrock transport in a Mountain stream: Bedload hysteresis and changing thresholds of motion. *Water Resources Research*, *56*(11), e2020WR028150. https://doi.org/10.1029/2020WR028150

Radice, A., Sarkar, S., & Ballio, F. (2017). Image-based lagrangian particle tracking in bed-load experiments. *Journal of Visualized Experiments: JoVE*, *125*, 55874. https://doi.org/10.3791/55874

Rebai, D., Radice, A., & Ballio, F. (2024). Traveling or jiggling: Particle motion modes and their relative contribution to bed-load variables. *Journal of Geophysical Research: Earth Surface*, *129*(8), e2024JF007637. https://doi.org/10.1029/2024JF007637

Recking, A., Liébault, F., Peteuil, C., & Jolimet, T. (2012). Testing bedload transport equations with consideration of time scales. *Earth Surface Processes and Landforms*, *37*(7), 774–789. https://doi.org/10.1002/esp.3213

Reid, I., Frostick, L. E., & Layman, J. T. (1985). The incidence and nature of bedload transport during flood flows in coarse-grained alluvial channels. *Earth Surface Processes and Landforms*, *10*(1), 33–44. https://doi.org/10.1002/esp.3290100107

Roseberry, J. C., Schmeeckle, M. W., & Furbish, D. J. (2012). A probabilistic description of the bed load sediment flux: 2. Particle activity and motions. *Journal of Geophysical Research: Earth Surface*, *117*(F3). https://doi.org/10.1029/2012JF002353

Roth, D. L., Finnegan, N. J., Brodsky, E. E., Cook, K. L., Stark, C. P., & Wang, H. W. (2014). Migration of a coarse fluvial sediment pulse detected by hysteresis in bedload generated seismic waves. *Earth and Planetary Science Letters*, *404*, 144–153. https://doi.org/10.1016/j.epsl.2014.07.019

Salevan, J. C., Clark, A. H., Shattuck, M. D., O'Hern, C. S., & Ouellette, N. T. (2017). Determining the onset of hydrodynamic erosion in turbulent flow. *Physical Review Fluids*, *2*(11), 114302. https://doi.org/10.1103/PhysRevFluids.2.114302

Seminara, G., Solari, L., & Parker, G. (2002). Bed load at low shields stress on arbitrarily sloping beds: Failure of the bagnold hypothesis. *Water Resources Research*, *38*(11), 31-1–31-16. https://doi.org/10.1029/2001WR000681

Shields, A. (1936). Application of similarity principles and turbulence research to bed-load movement.

Shim, J., & Duan, J. (2019). Experimental and theoretical study of bed load particle velocity. *Journal of Hydraulic Research*, *57*(1), 62–74. https://doi.org/10.1080/00221686.2018.1434837

Shim, J., & Duan, J. G. (2017). Experimental study of bed-load transport using particle motion tracking. *International Journal of Sediment Research*, *32*(1), 73–81. https://doi.org/10.1016/j.ijsrc.2016.10.002

Slotterback, S., Mailman, M., Ronaszegi, K., van Hecke, M., Girvan, M., & Losert, W. (2012). Onset of irreversibility in cyclic shear of granular packings. *Physical Review E*, *85*(2), 021309. https://doi.org/10.1103/PhysRevE.85.021309

Sumer, B. M., Chua, L. H. C., Cheng, N.-S., & Fredsøe, J. (2003). Influence of turbulence on bed load sediment transport. *Journal of Hydraulic Engineering*, *129*(8), 585–596. https://doi.org/10.1061/(ASCE)0733-9429(2003)129:8(585)

Toiya, M., Stambaugh, J., & Losert, W. (2004). Transient and oscillatory granular shear flow. *Physical Review Letters*, *93*(8), 088001. https://doi.org/10.1103/physrevlett.93.088001

Turowski, J. M., Badoux, A., & Rickenmann, D. (2011). Start and end of bedload transport in gravel-bed streams. *Geophysical Research Letters*, *38*(4). https://doi.org/10.1029/2010GL046558

Vanoni, V. A. (2006). Sediment transportation mechanics. *Sedimentation Engineering*, 11–189. https://doi.org/10.1061/9780784408230.ch02

Vericat, D., Batalla, R. J., & Garcia, C. (2006). Breakup and reestablishment of the armour layer in a large gravel-bed river below dams: The lower Ebro. *Geomorphology*, *76*(1–2), 122–136. https://doi.org/10.1016/j.geomorph.2005.10.005

Wiberg, P. L., & Dungan Smith, J. (1989). Model for calculating bed load transport of sediment. *Journal of Hydraulic Engineering*, *115*(1), 101–123. https://doi.org/10.1061/(ASCE)0733-9429(1989)115:1(101)

Wiberg, P. L., & Smith, J. D. (1987). Calculations of the critical shear stress for motion of uniform and heterogeneous sediments. *Water Resources Research*, *23*(8), 1471–1480. https://doi.org/10.1029/wr023i008p01471

Wong, M., & Parker, G. (2006). Reanalysis and correction of bed-load relation of Meyer-Peter and Müller using their own database. *Journal of Hydraulic Engineering*, *132*(11), 1159–1168. https://doi.org/10.1061/(asce)0733-9429(2006)132:11(1159)

Wong, M., Parker, G., DeVries, P., Brown, T. M., & Burges, S. J. (2007). Experiments on dispersion of tracer stones under lower-regime plane-bed equilibrium bed load transport. *Water Resources Research*, *43*(3). https://doi.org/10.1029/2006WR005172

Yager, E. M., Venditti, J. G., Smith, H. J., & Schmeeckle, M. W. (2018). The trouble with shear stress. *Geomorphology*, *323*, 41–50. https://doi.org/10.1016/j.geomorph.2018.09.008

Yang, H., Hu, X., Wang, S., Cheng, K., Luo, M., Wang, H., & Shi, J. (2024). The effect of stress history on the critical shear stress of bedload transport in gravel-bed streams. *Journal of Hydrology*, *645*, 132208. https://doi.org/10.1016/j.jhydrol.2024.132208